

## Combined effects of stress and temperature on hydrogen diffusion in non-hydride forming alloys applied in gas turbines

Zhang, Zhichao; Peeters, Jurriaan; Popovich, Vera; Ayas, Can

**DOI**

[10.1016/j.ijhydene.2022.07.006](https://doi.org/10.1016/j.ijhydene.2022.07.006)

**Publication date**

2022

**Document Version**

Final published version

**Published in**

International Journal of Hydrogen Energy

**Citation (APA)**

Zhang, Z., Peeters, J., Popovich, V., & Ayas, C. (2022). Combined effects of stress and temperature on hydrogen diffusion in non-hydride forming alloys applied in gas turbines. *International Journal of Hydrogen Energy*, 47(71), 30687-30706. <https://doi.org/10.1016/j.ijhydene.2022.07.006>

**Important note**

To cite this publication, please use the final published version (if applicable). Please check the document version above.

**Copyright**

Other than for strictly personal use, it is not permitted to download, forward or distribute the text or part of it, without the consent of the author(s) and/or copyright holder(s), unless the work is under an open content license such as Creative Commons.

**Takedown policy**

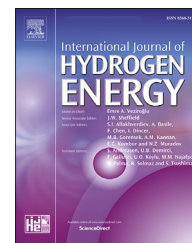
Please contact us and provide details if you believe this document breaches copyrights. We will remove access to the work immediately and investigate your claim.



ELSEVIER

Available online at [www.sciencedirect.com](http://www.sciencedirect.com)

ScienceDirect

journal homepage: [www.elsevier.com/locate/ijhe](http://www.elsevier.com/locate/ijhe)

# Combined effects of stress and temperature on hydrogen diffusion in non-hydride forming alloys applied in gas turbines

Zhichao Zhang<sup>a,b</sup>, Jurriaan Peeters<sup>a</sup>, Vera Popovich<sup>a</sup>, Can Ayas<sup>a,\*</sup>

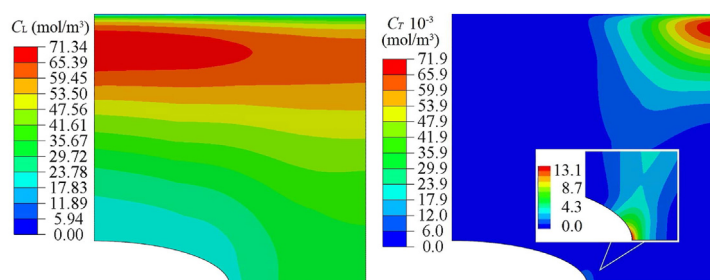
<sup>a</sup> Faculty of Mechanical, Maritime and Materials Engineering, Delft University of Technology, 2628CD Delft, the Netherlands

<sup>b</sup> Department of Mechanical and Construction Engineering, Faculty of Engineering and Environment, Northumbria University, Newcastle upon Tyne, NE1 8ST, UK

## HIGHLIGHTS

- Stress and temperature gradients are accounted for estimating hydrogen distribution in non-hydride forming alloys.
- Temperature gradients in turbine blades are the most prominent factor for the susceptibility of hydrogen embrittlement.
- The average temperature or the direction of the temperature gradient can be modified to reduce the risk of embrittlement.

## GRAPHICAL ABSTRACT



## ARTICLE INFO

### Article history:

Received 17 January 2022

Received in revised form

27 June 2022

Accepted 2 July 2022

Available online 16 August 2022

### Keywords:

Hydrogen diffusion

Stress

Temperature

Finite element analysis

Gas turbine

Alloy 690

## ABSTRACT

Hydrogen plays a vital role in the utilisation of renewable energy, but ingress and diffusion of hydrogen in a gas turbine can induce hydrogen embrittlement on its metallic components. This paper aims to investigate the hydrogen transport in a non-hydride forming alloy such as Alloy 690 used in gas turbines inspired by service conditions of turbine blades, i.e. under the combined effects of stress and temperature. An appropriate hydrogen transport equation is formulated, accounting for both stress and temperature distributions of the domain in the non-hydride forming alloy. Finite element (FE) analyses are performed to predict steady-state hydrogen distribution in lattice sites and dislocation traps of a double notched specimen under constant tensile load and various temperature fields. Results demonstrate that the lattice hydrogen concentration is very sensitive to the temperature gradients, whilst the stress concentration only slightly increases local lattice hydrogen concentration. The combined effects of stress and temperature result in the highest concentration of the dislocation trapped hydrogen in low-temperature regions, although the plastic strain is only at a moderate level. Our results suggest that temperature

\* Corresponding author.

E-mail address: [c.ayas@tudelft.nl](mailto:c.ayas@tudelft.nl) (C. Ayas).

<https://doi.org/10.1016/j.ijhydene.2022.07.006>

0360-3199/© 2022 The Author(s). Published by Elsevier Ltd on behalf of Hydrogen Energy Publications LLC. This is an open access article under the CC BY license (<http://creativecommons.org/licenses/by/4.0/>).

gradients and stress concentrations in turbine blades due to cooling channels and holes make the relatively low-temperature regions susceptible to hydrogen embrittlement.

© 2022 The Author(s). Published by Elsevier Ltd on behalf of Hydrogen Energy Publications LLC. This is an open access article under the CC BY license (<http://creativecommons.org/licenses/by/4.0/>).

## Introduction

Hydrogen is an essential renewable fuel for gas turbines to generate electricity owing to its high energy content and no carbon dioxide emission [1,2]. The utilisation of hydrogen is limited due to the high costs in storage and transportation, e.g., liquefaction and resistance to leakage, as well as higher emission level of nitric oxides, which have been investigated previously; see for example [3,4]. However, hydrogen embrittlement with its commonly observed adverse effect on mechanical reliability is another challenge for applying hydrogen fuel in gas turbines, which may influence the longevity of gas turbine components and induce safety issues.

Hydrogen embrittlement is the reduction of ductility and toughness of metals in the presence of a small amount of hydrogen, which can induce sudden premature failure [5,6] or hydrogen-assisted fatigue, e.g. Refs. [7,8]. Consequently, the interaction of hydrogen gas with, for instance, turbine blades and the distribution of hydrogen concentration therein is of paramount importance. Nickel-based alloys are non-hydride forming alloys that are widely used for turbine blades since they can resist high stress at high temperatures [9]. In these non-hydride forming alloys, hydrogen transport occurs by the movement of hydrogen atoms through the normal interstitial lattice sites. In contrast, some hydrogen is trapped at microstructural defects such as dislocations, grain boundaries and carbide interfaces [10,11]. Various mechanisms for hydrogen embrittlement have been proposed, and the role of lattice and trapped hydrogen is rationalised with a specific hydrogen embrittlement mechanism. However, in terms of gas turbines, so far, only the sensitivity of material properties of nickel containing alloys to the external high hydrogen gas pressure and high uniform temperature was assessed [12], where the specimen was regarded as dimensionless, and its internal distribution of hydrogen in different sites was not accounted. Consequently, it is of interest to investigate hydrogen diffusion in lattice and trapping sites of nickel-based alloys under typical service conditions of turbine blades for power generation. This corresponds to hydrogen diffusion in the presence of both a temperature gradient and a stress gradient, as a revolving turbine blade is subject to hot gas and cooling air as well as the non-uniform tensile stress induced by the centrifugal force [13,14].

It is well known that the diffusion of hydrogen is strongly influenced by hydrostatic stress [15–17]. Barrera et al. [18] performed finite element calculations accounting for the stress-mediated diffusion of lattice hydrogen and demonstrated the effect of hydrostatic stress on the hydrogen distribution of notched specimens under remote tensile stress. Recently, Shang et al. [19] conducted slow strain rate tensile

tests and finite element analyses on X70 steel notched specimens with different stress concentration factors (maximum stress over remote nominal stress) in 10 MPa nitrogen/hydrogen mixtures. It was found that the maximum hydrogen concentration occurs at the notch tip where the stress is concentrated, and its value increases with the increased stress concentration factor. Moreover, their finite element model demonstrated that the location of the maximum hydrogen concentration in lattice sites moves from the notch tip to the front of the notch tip with the increasing tensile load, whilst the trapped hydrogen peak stays at the notch tip. However, the influence of temperature on lattice hydrogen diffusion was not considered, i.e. both of these studies were undertaken at room temperature. Given that most material properties such as hydrogen diffusivity, solubility, elastic modulus, yield strength and strain hardening are temperature dependent [20,21], the hydrogen concentration in metals is undoubtedly affected by temperature. Moreover, it is well established that the temperature gradient acts as a driving force for lattice hydrogen diffusion [22–24]. However, these studies were conducted in the absence of loading and hence did not consider the effect of stress on hydrogen diffusion. Varias et al. [25] and Quecedo et al. [26] investigated hydrogen embrittlement accounting for the influences of temperature and stress on nuclear reactors. Nevertheless, these studies all focused on the formation of hydrides in materials such as Zirconium alloys. In contrast, gas turbines typically comprise nickel-based alloys for creep resistance. Nickel-based alloys are non-hydride forming, in which hydrogen embrittlement occurs with no hydride formation [18,27,28]. Therefore, this paper will focus on the hydrogen diffusion in non-hydride forming alloys under the influences of both stress and temperature.

Previously, we mentioned that hydrogen also exists at traps beside the interstitial sites of the lattice. However, the role of hydrogen that is trapped at the microstructural defects is a controversial issue. For example, Novak et al. [29] regarded hydrogen trapped at dislocations to be essential and conjectured a decrease in the length of dislocation pile-ups at carbide particles due to hydrogen enhanced local plasticity (HELP) mechanism. This, in turn, decreases the cohesive strength of the carbide interface and thereby reduces the macroscopic ductility of high-strength steels. Nagao et al. [30] also adopted this idea and verified it using a series of experiments. However, investigations on a similar high strength steel grade directly correlated the lattice hydrogen concentration and degree of embrittlement [31,32], and also fracture strength of tensile specimens charged with various amounts of hydrogen were independent of the hydrogen trapped at dislocations, grain boundaries and carbides [31,33]. More recently, Shishvan et al. [34] tried to

resolve this controversy by proposing the hydrogen-induced fast fracture mechanism. According to this mechanism, all hydrogen atoms in a microscopic cavity of a specimen are consumed to form hydrides on the cavity surfaces, promoting fast crack propagation. The crack continues to propagate fast to cause cleavage fracture without hydrogen present as long as the tensile stress is at an appropriate level. Supported by detailed atomistic and continuum calculations, the fast fracture hypothesis can explain well-established experimental observations along with the insensitivity of the strength to the trapped hydrogen concentration. Nevertheless, this is a hydride forming mechanism and is not applicable to non-hydride forming alloys, which means the role of trapped hydrogen in non-hydride forming alloys may be different.

In summary, hydrogen diffusion influenced by stress and temperature simultaneously has not been studied for non-hydride forming alloys, where the severity of hydrogen embrittlement highly depends on the transport of lattice hydrogen and the distribution of trapped hydrogen. The nickel-based Alloy 690 is a non-hydride forming material [18] extensively used in combustion systems and turbines [35]. Therefore, this study investigates the steady-state hydrogen distribution in Alloy 690 under conditions inspired by a hydrogen-powered turbine blade. A new hydrogen transport equation is developed, and finite element (FE) analysis is performed, which are applicable to hydrogen diffusion in non-hydride forming alloys subjected to non-uniform stress field and non-uniform temperature field simultaneously. The outcomes of this research would be essential to evaluate the most susceptible regions in gas turbines to hydrogen embrittlement when using hydrogen as the fuel for electricity generation.

## Theory of hydrogen transport

In this section, we firstly formulate the stress and temperature mediated transport equation of lattice hydrogen concentration  $C_L$ . Subsequently, we summarise how the trapped hydrogen concentration  $C_T$  can be estimated using Oriani theory [22] while accounting for temperature variation.

### Hydrogen transport equation

The chemical potential gradient of the lattice hydrogen constitutes a driving force for the lattice hydrogen flux  $\mathbf{j}$ , which is given as

$$\mathbf{j} = -\frac{D_L C_L}{RT} \nabla \mu, \quad (1)$$

where  $D_L$  is lattice diffusivity given in units of  $\text{m}^2/\text{s}$ ,  $C_L$  is lattice hydrogen concentration given in units of  $\text{mol}/\text{m}^3$ ,  $R = 8.31 \text{ J}/(\text{mol K})$  is the gas constant,  $T$  is temperature given in the units of K, and  $\mu$  is chemical potential at constant temperature given in the units of  $\text{J}/\text{mol}$ . In order to account for the effect of stress besides lattice hydrogen concentration gradient, chemical potential can be written as

$$\mu = \mu_0 + RT \ln C_L - \sigma_H V_H. \quad (2)$$

Here  $\mu_0$  is the standard state chemical potential.  $V_H$  is the partial molar volume of hydrogen given in units of  $\text{m}^3/\text{mol}$ . The hydrostatic stress is denoted by  $\sigma_H$  and given as  $\sigma_H = (\sigma_{11} + \sigma_{22} + \sigma_{33})/3$  in units of Pa, where  $\sigma_{11}$ ,  $\sigma_{22}$  and  $\sigma_{33}$  are the normal stress components of the stress tensor. Thus, the lattice hydrogen flux can be written as

$$\mathbf{j} = -\frac{D_L C_L}{RT} \nabla \mu = -\frac{D_L C_L}{RT} (RT \nabla \ln C_L - V_H \nabla \sigma_H). \quad (3)$$

Here,  $RT \nabla \ln C_L$  and  $V_H \nabla \sigma_H$  are the driving forces for diffusion generated by the concentration gradient and the hydrostatic stress gradient, respectively. However, since the chemical potential given in Eq. (2) is valid for constant temperature, Eq. (3) is not suitable when the temperature is non-uniform or non-steady. An additional driving force that is associated with temperature gradients is introduced, and the corresponding flux of hydrogen in a thermotransport process is governed by

$$\mathbf{j} = -\frac{D_L C_L}{RT} (\nabla \mu + Q^* \nabla \ln T) = -\frac{D_L C_L}{RT} \left( RT \nabla \ln C_L + \frac{Q^*}{T} \nabla T \right), \quad (4)$$

in the absence of loading, i.e. omitting the term  $-\sigma_H V_H$  in Eq. (2) [22,36,37]. In Eq. (4),  $(Q^*/T) \nabla T$  is the driving force for diffusion generated by temperature gradient, and  $Q^*$  is the heat of transport given in units  $\text{J}/\text{mol}$  that can be determined experimentally [22,23]. Upon combining Eqs. (3) and (4) to account for all driving forces of interest for lattice hydrogen diffusion, we arrive at

$$\mathbf{j} = -\frac{D_L C_L}{RT} \left( RT \nabla \ln C_L - V_H \nabla \sigma_H + \frac{Q^*}{T} \nabla T \right). \quad (5)$$

The conservation of mass dictates

$$\frac{\partial C}{\partial t} + \nabla \cdot \mathbf{j} = 0, \quad (6)$$

where  $t$  is time and  $C$  is the total hydrogen concentration  $C = C_L + C_T$  (concentration of lattice hydrogen  $C_L$  and trapped hydrogen  $C_T$ ). Consequently, the transient form of hydrogen transport equation can be written as

$$\frac{\partial (C_L + C_T)}{\partial t} - \nabla \cdot D_L \left( \nabla C_L - \frac{V_H C_L}{RT} \nabla \sigma_H + \frac{Q^* C_L}{RT^2} \nabla T \right) = 0. \quad (7)$$

Equation (7) accounts for the lattice hydrogen transport driven by lattice hydrogen concentration gradient, hydrostatic stress gradient as well as temperature gradient. The steady-state form of Equation (7) is obtained when  $\partial C/\partial t = 0$ ,

$$\nabla \cdot D_L \left( \nabla C_L - \frac{V_H C_L}{RT} \nabla \sigma_H + \frac{Q^* C_L}{RT^2} \nabla T \right) = 0. \quad (8)$$

Next, the lattice hydrogen concentration  $C_L$  can be replaced by the normalised concentration  $\phi$  using the equation  $\phi = C_L/s$ . Here  $s$  is the solubility constant in units of  $\text{mol}/(\text{m}^3 \sqrt{\text{Pa}})$ , which depends on temperature and base material [38]. Equation (8) then becomes

$$\nabla \cdot sD_L \left( \nabla \phi - \frac{V_H \phi}{RT} \nabla \sigma_H + \left( \frac{C_L}{s^2} \frac{ds}{dT} + \frac{Q^* \phi}{RT^2} \right) \nabla T \right) = 0. \quad (9)$$

### Hydrogen at trapping sites

Previously we mentioned that hydrogen either resides in the interstitial sites denoted with  $C_L$  or is trapped at the microstructural defects denoted with  $C_T$ . In this paper, we only consider the trapped hydrogen at dislocations because the hydrogen concentration at grain boundaries, carbides, etc., are insensitive to the local lattice hydrogen concentration [31]. The expressions for lattice hydrogen concentration and trapped hydrogen concentration are given as

$$C_L = \beta \theta_L \frac{N_L}{N_A}, \quad (10)$$

$$C_T = \alpha \theta_T \frac{N_T}{N_A}. \quad (11)$$

Here,  $\beta$  is the number of lattice sites per solvent atom,  $\alpha = 1$  denotes the number of trapping sites,  $\theta_L$  and  $\theta_T$  are the fraction of lattice sites and trapping sites occupied by hydrogen atoms, respectively, that are bounded as  $0 \leq \theta_L \leq 1$  and  $0 \leq \theta_T \leq 1$ .  $N_A = 6.023 \times 10^{23}$  atoms/mol is the Avogadro's number,  $N_L$  is the number of atoms of solvent per unit volume (atoms/m<sup>3</sup>), which is a constant that depends on the type of base material.  $N_T$  denotes the number of atomic trapping sites along the total dislocation line length per unit volume (atoms/m<sup>3</sup>), and its value is proportional to the dislocation density  $\rho^d$  (m<sup>-2</sup>) [18], i.e.

$$N_T = \frac{\sqrt{2}}{a} \rho^d, \quad (12)$$

where  $a$  is the lattice constant (m) of the material, and  $\rho^d$  is a function of the accumulated Von Misses plastic strain  $\epsilon^p$ :

$$\rho^d = \begin{cases} \rho_0^d + \gamma \epsilon^p, & \epsilon^p < 0.5 \\ 10^{16}, & \epsilon^p \geq 0.5 \end{cases} \quad (13)$$

Barrera et al. [18] suggests  $\rho_0^d = 10^{10}$  m<sup>-2</sup> for the material Alloy 690, and  $\gamma$  is a constant which is equal to  $2 \times 10^{16}$  m<sup>-2</sup>. According to Oriani's theory [11], the hydrogen concentration in the lattice sites is in equilibrium with that at the reversible trapping sites. The relationship between them can be described by:

$$\frac{1 - \theta_L}{\theta_L} \frac{\theta_T}{1 - \theta_T} = K, \quad (14)$$

where  $K$  is the equilibrium constant determined by the binding energy for the traps  $W_B$  as

$$K = e^{-\frac{W_B}{RT}}. \quad (15)$$

$W_B = -18$  kJ/mol for the dislocation [29]. For  $\theta_L \ll 1$ ,

$$\frac{\theta_T}{1 - \theta_T} = K \theta_L. \quad (16)$$

Substituting Eq. (16) and Eq. (12) into Eq. (11),  $C_T$  is finally expressed as:

$$C_T = \frac{\sqrt{2} K C_L \rho^d}{a(\beta N_L + K N_A C_L)}. \quad (17)$$

### Mechanical equilibrium

In order to solve the hydrogen transport equation, knowledge of the hydrostatic stress field is required. For that purpose, a mechanical boundary value problem has to be solved. The governing equation for static equilibrium, neglecting body forces in the solid, is stated as

$$\text{div}(\sigma) = 0 \quad (18)$$

where  $\sigma$  is the Cauchy stress tensor which is related to the traction vector

$$\mathbf{t} = \sigma \mathbf{n}. \quad (19)$$

Here,  $\mathbf{n}$  is the outward normal unit vector at the point of interest. Linear isotropic elasticity and  $J_2$  flow theory with isotropic hardening are employed as the constitutive behaviour.

### Thermal equilibrium

The solution of the hydrogen transport equation given above also requires knowledge of the temperature field, which can be obtained by solving a thermal boundary value problem that is governed by the conservation of energy

$$\frac{\partial T}{\partial t} = \frac{1}{\rho c_p} \nabla \cdot \mathbf{q}, \quad (20)$$

where  $T$  is the temperature,  $t$  is the time,  $\rho$  is the density and  $c_p$  is the heat capacity. The heat flux  $\mathbf{q}$  is given as

$$\mathbf{q} = -k \nabla T. \quad (21)$$

Here  $k$  is the thermal conductivity of isotropic material. Combining Eq. (20) and Eq. (21) for steady-state yields

$$\nabla^2 T = 0. \quad (22)$$

### Finite element (FE) analysis

Under the working conditions of turbine blades, centrifugal forces on the typical geometry of the blade generate a non-uniform stress field with hydrostatic stress predominantly tensile in nature. The stress distribution is considered time-independent and instantaneous since the rate of elastoplastic deformation is much higher than that of hydrogen diffusion. Moreover, a non-uniform temperature field is assumed for the blade since it is in contact with a hot atmosphere while internally cooled through conformal cooling channels. Upon comparing the mean conduction length  $\sqrt{\alpha t}$  and mean diffusion length  $\sqrt{Dt}$  for unit time, it is apparent that temperature distribution reaches a steady-state much earlier than that of hydrogen concentration. Consequently, it is reasonable to neglect the temperature transients and use the steady-state temperature distribution for stress

and hydrogen concentration prediction under these circumstances.

Our methodology can be summarised as follows. First, a one-way coupled thermo-mechanical boundary value problem is solved by FE analysis to attain the steady-state temperature field and the corresponding mechanical field quantities. One-way coupling implies the mechanical boundary value problem of an elastoplastic material makes due account of the steady-state temperature field of the domain. Subsequently, a separate FE analysis is performed for the hydrogen transport governed by Eq. (9), accounting for both the established temperature field and the hydrostatic stress distribution in the solid. Note that the influence of hydrogen concentration on mechanical properties is not accounted for in this study for simplicity. Moreover, the degree of knockdown in yield strength and the exact mechanism of how the lattice and trapped hydrogen change the local yield strength is controversial (see for example [29,31,32,34]) and also material specific.

All calculations are performed with the commercial FE program ABAQUS 2019. In ABAQUS, the mass transport equation has the form

$$\nabla \cdot sD_L (\nabla \varphi - K_p \nabla \sigma_H + K_s \nabla \ln T) = 0. \quad (23)$$

Here,  $K_s$  and  $K_p$  are the Soret effect and pressure effect factors. By comparing Eq. (23) with Eq. (9), we obtain

$$K_p = \frac{V_H \varphi}{RT}, \quad (24)$$

and

$$K_s = \frac{C_L T}{s^2} \frac{ds}{dT} + \frac{Q^* \varphi}{RT}. \quad (25)$$

Consequently, lattice hydrogen concentration ( $C_L = \varphi s$ ) is obtained by solving Eq. (23), whilst trapped hydrogen concentration is calculated using Eq. (17) as a post-processing step.

## Model verification and validation

In order to verify the current model and its numerical implementation in ABAQUS 2019, the lattice hydrogen distributions in two cases from Barrera et al. [18] are compared with the predictions of the above described FE analysis. The first case is a 2D square plate (120 mm  $\times$  120 mm) with a circular hole (radius  $r = 4$  mm) at the centre, under plane stress conditions in the elastic regime. Since this case does not account for the influence of plasticity and trapping sites, another case is used which is a 2D plate (120 mm  $\times$  120 mm) with elliptical notches (major axis = 40 mm, minor axis = 10 mm) under plane stress and plastic deformation.

In the first case [18], an evenly distributed normal tensile traction of 100 MPa is applied on the top surface of the plate with no tangential traction. Barrera et al. [18] considered a duration of  $10^{10}$  s for the diffusion under room temperature, which implies that the steady-state for hydrogen concentration is established. Note that, since the temperature is uniform and remains as such with time, a thermo-mechanical coupling is not necessary. Initially, the plate has a uniform

lattice hydrogen concentration of  $C_L = 20$  mol/m<sup>3</sup>. The symmetry boundary conditions are prescribed on the left and bottom boundaries of the quarter of the square plate shown in Fig. 1a, both for the mechanical and the diffusion boundary value problems. The top and right boundaries of the plate are material flux free while the right boundary is also traction free. The second case [18] in Fig. 1b has similar boundary conditions such that the symmetry boundary condition applies to right and bottom boundaries, the left boundary is traction and flux free, and the top edge is subjected to 0.6 mm displacement in the  $x_2$  direction while it is traction free in the  $x_1$  direction. In the second case, the specimen undergoes elastoplastic deformation and the initial hydrogen concentration is  $C_L = 27$  mol/m<sup>3</sup>. In Fig. 1, contour levels of steady-state lattice hydrogen distribution of our FE analyses are given. In Table 1,  $C_L$  values predicted with the current FE analysis are compared with the data reported by Barrera et al. [18] at five selected locations labelled as A, B, C, D and E in Fig. 1. The discrepancy for predicted  $C_L$  at Points A, C and D are 0.75%, 0.86% and 6.8%, respectively. The discrepancy in lattice hydrogen concentrations at Point D is larger compared with that at A and C as anticipated because the influence of hydrogen concentration on yield strength is not accounted for in our model in contrast to Barrera et al. [18]. Consequently, the plastic strain and the trapped hydrogen concentration are slightly different from what is reported in Barrera et al. [18]. Here, Points A and D correspond to the locations where the highest tensile hydrostatic stress is attained in the two cases, whilst Point C is the location under the lowest compressive hydrostatic stress.

Next, the current model is verified for hydrogen diffusion that occurs over a non-uniform temperature field in the absence of a loading. Longhurst [39] considered diffusion of tritium (an isotope of hydrogen) across a 316 stainless steel wall of 0.5 cm thickness where a uniform temperature of 673 K and a uniform concentration of  $C_L = 1.41$  wt.ppm (11.14 mol/m<sup>3</sup>) are maintained at one side of the wall a uniform temperature of 373 K, and a uniform concentration of  $C_L = 0$  are retained on the other side of the wall. This time in the absence of any loading, a mechanical boundary value problem is not needed. Material properties of tritium used in our calculation are reported in Table A1 in Appendix A. Fig. 2a depicts the tritium concentration as a function of normalised distance at steady-state. A reasonably good agreement is attained between the prediction of the Longhurst [39] and the current model.

In Fig. 2b, we validate the predictions of our FE analysis with the experimental measurements reported in the literature. Kim et al. [36], considered a specimen of modified Zircaloy-4 alloy, which initially has a uniform concentration of 91.7 wt.ppm (601.55 mol/m<sup>3</sup>) hydrogen. The two ends of this specimen were kept at 300 °C and 340 °C, respectively, for 35 days. Although the Zircaloy-4 is a hydride forming alloy, there is no hydride in the region where the temperature is between 320 °C and 340 °C (between 12 and 24 mm from the cold surface). Consequently, the equation proposed in this paper can still be used to calculate hydrogen concentration in this specific region. Results obtained in Fig. 2b demonstrate a good agreement between the current FE model and the experimental measurements.

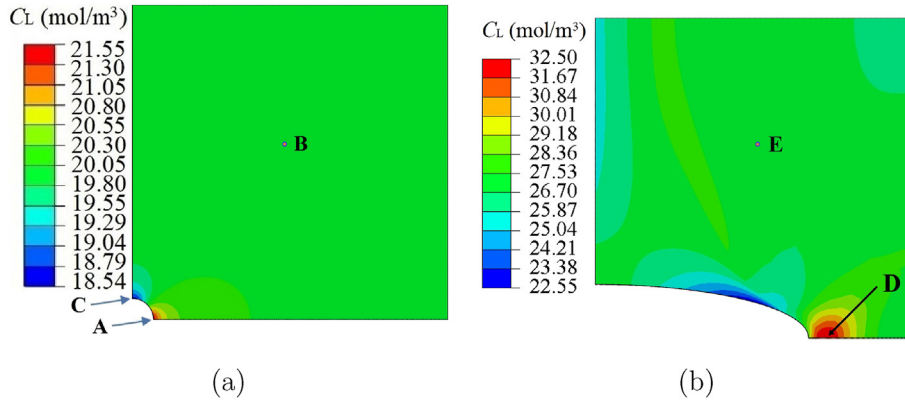


Fig. 1 – Distribution of lattice hydrogen concentration (a) for the quarter of a square plate with a hole and (b) for the quarter of a notched plate as described in Barrera et al. [18].

Table 1 – Comparison of lattice hydrogen concentration in units of mol/m<sup>3</sup> predicted by the current model and as reported by Barrera et al. [18] at points A, B, C, D and E labelled in Fig. 1.

Point	Current model	Barrera et al.	Discrepancy
A	21.55	21.39	0.75%
B	20	20	0
C	18.54	18.7	0.86%
D	32.50	34.88	6.8%
E	27	27	0

**Numerical examples**

It remains to investigate the combined effects of stress and temperature on hydrogen transport. For this purpose, we consider a 2D double notched specimen under plane strain. The quarter of the specimen shown in Fig. 3 is sufficient for FE analyses due to two axes of symmetry indicated with dashed-dotted lines in Fig. 3 along with the dimensions of the domain. Consequently, the right and bottom boundaries are prescribed with symmetry boundary conditions for the thermal,

mechanical and diffusion boundary value problems. A structured FE mesh comprising linear quadrilateral elements is employed. The FE mesh is refined to a size of 0.17 mm × 0.10 mm in the proximity of the notch root to capture the steep gradients of the hydrostatic stress due to stress concentration, and the total number of elements is 26,825. The mesh convergence study is depicted in Fig. B1 in Appendix B, revealing this mesh density ensures a high level of numerical accuracy. The material properties representative of the Alloy 690 are listed in Table 2. Young's modulus [40] and plastic hardening response [41] as a function of temperature are given in Appendix C in Fig. C1 and Fig. C2, respectively. The effect of strain rate on strain hardening of Alloy 690 is negligible in the temperature range 298–1073 K [40].

The temperature in the specimen is initially uniform and set to 300 K. A non-uniform temperature distribution is induced by prescribing selected values of fixed temperature at the notch surface  $T_{Notch}$  and the top boundary  $T_{Top}$  ranging between 300 K and 900 K. The values for  $T_{Notch}$  and  $T_{Top}$  for all cases considered in this study are tabulated in Table 3. The left boundary of the domain is always thermally insulated. We define  $\eta = (T_{Top} - T_{Notch})/L$ , which characterises the global temperature gradient imposed on the domain. Here,

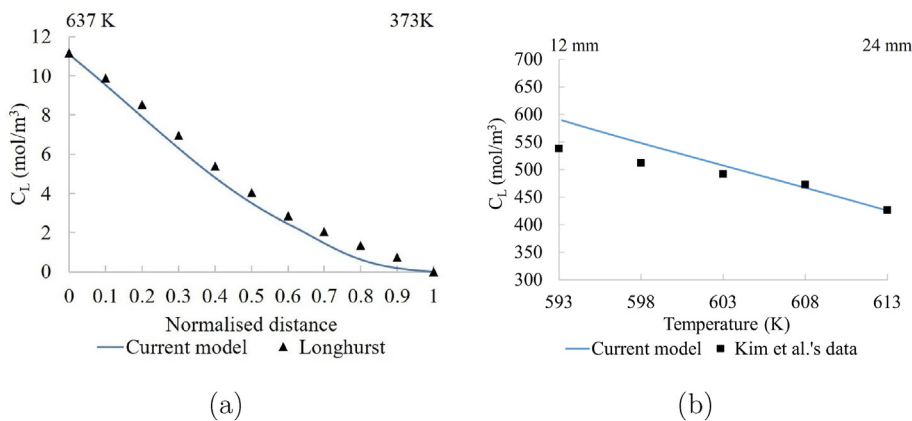
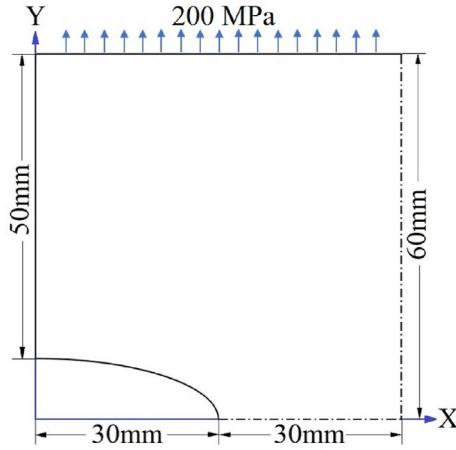


Fig. 2 – Distribution of hydrogen concentration obtained by current model superimposed with (a) predictions reported by Longhurst [39] with temperatures at the two ends of the specimen and (b) experimental measurements of Kim et al. [36] within the region of the specimen without hydrides.



**Fig. 3 – Dimensions of the quarter of the double notched specimen and the applied loading. The dashed-dotted lines indicate the axes of symmetry.**

**Table 2 – Material properties of Alloy 690.**

Parameter	Value
$\rho$ (kg/m <sup>3</sup> )	$8.19 \times 10^3$
$N_L$ (m <sup>-3</sup> )	$9.24 \times 10^{28}$
$D_L$ (m <sup>2</sup> /s)	$6.87 \times 10^{-7} \exp\left(-\frac{50700}{RT}\right)$ [42]
$s$ (mol/(m <sup>3</sup> √MPa))	$537.52 \exp\left(-\frac{9615.77}{RT}\right)$ [38]
$E$	See Fig. C1 [41]
$\sigma_y$	See Fig. C2 [40]
$\nu$	0.3
$V_H$ (m <sup>3</sup> /mol)	$2 \times 10^{-6}$
$W_B$ (kJ/mol)	-18
$a$ (m)	$2.86 \times 10^{-10}$
$\beta$	6
$Q^*$ (J/mol)	3976 [39]

$L = 50$  mm is the distance between the notch surface and the top surface at the left edge of the specimen. We also define  $\bar{T} = (T_{\text{Top}} + T_{\text{Notch}})/2$  as an indication of the average temperature at the steady-state. The values of  $\eta$  and  $\bar{T}$  are also tabulated in Table 3.

The double notched specimen is subjected to an evenly distributed normal traction of 200 MPa with no tangential traction at the top surface. The left boundary of the domain and the notch surface are traction free.

The initial lattice hydrogen concentration is  $C_L = 0$  everywhere in the specimen. The hydrogen concentration at the notch surface is prescribed to  $C_L = 20$  mol/m<sup>3</sup>, whilst at the top surface, lattice hydrogen concentration is prescribed to  $C_L = 0$  for all cases.

Apart from the 12 cases with non-uniform temperature distribution, three reference cases (Ref. 1, Ref. 2 and Ref. 3) are defined with a uniform temperature of 300 K, 900 K and 600 K, respectively.

For all cases, a thermo-mechanical analysis is performed with the 8-node quadratic, reduced integration elements (CPE8RT in ABAQUS). Given the fact that hydrogen diffusion is much slower than both the elastoplastic mechanical

**Table 3 – Thermal boundary conditions for the numerical examples considered in the study.**

Case	Variable	$T_{\text{Notch}}$ (K)	$T_{\text{Top}}$ (K)	$\eta$ (K/mm)	$\bar{T}$ (K)
Ref. 1	$T$	300	300	0	300
Ref. 2		900	900		900
Ref. 3		600	600		600
1	$\bar{T}$	500	300	-4	400
2		700	500	-4	600
3		900	700	-4	800
4		300	500	4	400
5		500	700	4	600
6		700	900	4	800
7	$\eta$	900	300	-12	600
8		800	400	-8	600
9		700	500	-4	600
10		300	900	12	600
11		400	800	8	600
12		500	700	4	600

response and the heat transfer, the hydrostatic stress and temperature fields obtained from the thermo-mechanical analysis are incorporated into the steady-state mass diffusion analysis. The hydrogen diffusion analysis is undertaken using 8-node quadratic quadrilateral elements (DC2D8 in ABAQUS). Ni-based alloys used for turbine blades have high creep resistance. At the highest temperature of 900 K and constant applied loading of 200 MPa considered in our study, the creep rate of Alloy 690 ranges is between 0.0001/hr and 0.0005/hr [43] which is negligible for the hydrogen diffusion. Therefore, the influence of creep is not accounted for in this paper.

## Results and discussion

In this section, the combined effects of temperature and stress on steady-state hydrogen concentration in lattice and at trapping sites are investigated through the cases that have been described in the previous section.

### Hydrogen transport at a uniform temperature

We first look at the effect of uniform temperature on the steady-state lattice hydrogen distribution. Fig. 4 shows the distribution of hydrostatic stress for the two reference cases: Case Ref. 1 when  $T = 300$  K (Fig. 4a) and Case Ref. 2 when  $T = 900$  K (Fig. 4b). In both cases, the hydrostatic stress is predominantly tensile. It reaches its maximum value in the close vicinity of the notch root precisely at the boundary of the plastic zone (e.g., see Point A in Fig. 4). Moreover, the variation of hydrostatic stress is more pronounced along the  $X$  – axis for Case Ref. 1 compared to Case Ref. 2. This implies a steeper gradient of hydrostatic stress in the  $X$  direction when  $T = 300$  K compared with the case when  $T = 900$  K. Note that yield strength decreases when  $T = 900$  K is due to thermal softening, leading to more plasticity and thereby more stress relaxation around the notch.

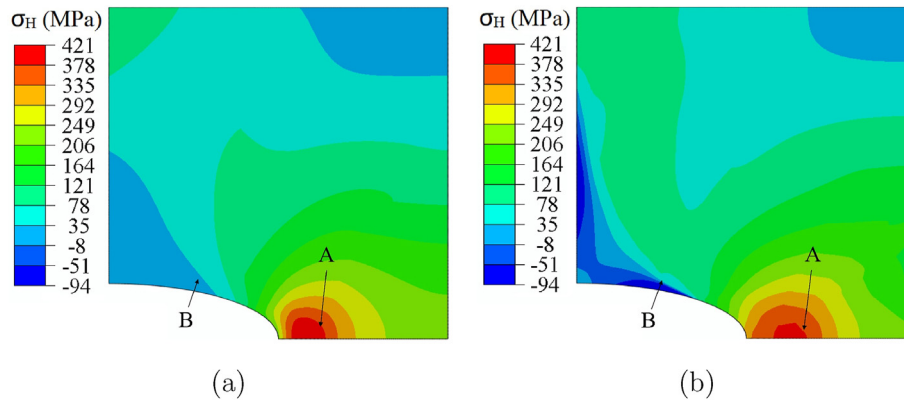


**Fig. 4 – Hydrostatic stress field of the double notched specimen and under tension for (a) Case Ref. 1 when  $T = 300$  K and (b) for Case Ref. 2 when  $T = 900$  K.**

The lowest value of compressive hydrostatic stress is near the bottom left corner of the domain, above the notch flank. The origin of this compressive hydrostatic stress is the displacement of material points in the diagonal direction towards the top right corner of the specimen. Point B labelled in Fig. 4a is located on the boundary where the nature of hydrostatic stress turns from tensile to compressive. In Fig. 4b, i.e. when  $T = 900$  K, this transition occurs more distinctly, and the magnitude of the lowest compressive  $\sigma_H$  increases. Just above the notch flank, the increase in the magnitude of local deformation overcompensates the decrease in  $E$  when the temperature rises to 900 K under the fixed remote loading of 200 MPa at the top surface.

The corresponding steady-state lattice hydrogen concentrations are given in Fig. 5. Both in Fig. 5a and 5b when  $T = 300$  K and  $T = 900$  K, respectively, the maximum lattice hydrogen concentration is  $21.23 \text{ mol/m}^3$ . Note that,  $\nabla T = 0$  for uniform temperature in Eq. (8). Also, recall that the term associated with hydrostatic stress becomes more pronounced when the temperature is reduced. Consequently, the  $C_L$  distributions in Fig. 5a and 5b are slightly different due to slightly different  $\sigma_H$  distributions and the different temperature levels. For instance, when  $T = 300$  K, a tiny plastic zone forms along the  $X$  – axis, and thus steep hydrostatic stress gradients exist in the  $X$  direction. Consequently, a larger region that accumulates a high concentration of lattice hydrogen is seen in

Fig. 5a. Moreover, in Fig. 5b, when  $T = 900$  K, the isoline with the highest value of  $C_L$  at the rim of the notch extends to where (see Point B in Figs. 4b and 5b) the compressive  $\sigma_H$  turns into tensile, i.e. where the gradient of  $\sigma_H$  is high.

Next, we investigate the hydrogen trapped at dislocations for the double notched specimen. Previously we showed that the trapped hydrogen concentration given with Eq. (16) is a function of plastic strain, temperature, and lattice hydrogen concentration. The distribution of Von-Mises plastic strain for Case Ref. 1 when  $T = 300$  K and for Case Ref. 2 when  $T = 900$  K is given in Fig. 6a and Fig. 6b, respectively. It can be observed that plastic strain is predominantly present at the notch root due to stress concentration and at the top right corner of the domain. Moreover, the equivalent plastic strain at the notch root increases approximately 12 fold from  $e^p = 0.0284$  to  $e^p = 0.358$  when the temperature rises from 300 K to 900 K. This is due to i) reduction of the yield strength from 260 MPa to 130 MPa and ii) reduction of the degree of plastic hardening (see Fig. C2 in Appendix).

In Fig. 7, the distribution of  $C_T$  for Case Ref. 1 when  $T = 300$  K and for Case Ref. 2 when  $T = 900$  K is given. It is observed that the trapped hydrogen at dislocations mainly accumulates near the notch root for both cases and  $C_T$  in Case Ref. 1 when  $T = 300$  K is nearly an order of magnitude higher than that in Case Ref. 2 when  $T = 900$  K. This can be rationalised by Eq. (16). Despite a larger plastic strain prevailing in Case Ref. 2, the

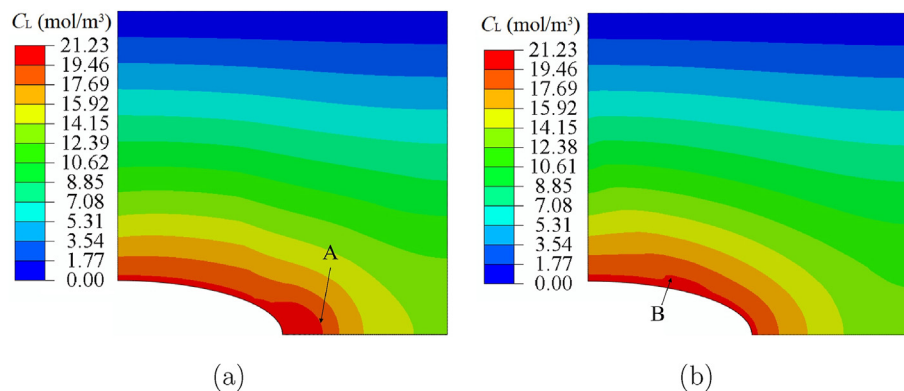


**Fig. 5 – Lattice hydrogen concentration distribution of the double notched specimen and under tension for (a) Case Ref. 1 when  $T = 300$  K and (b) for Case Ref. 2 when  $T = 900$  K.**

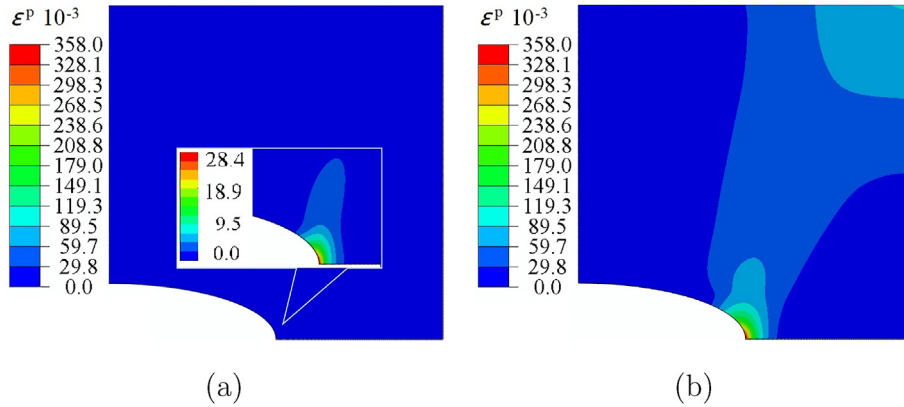


**Fig. 6** – Von-Mises equivalent plastic strain in the double notched specimen under tension (a) for Case Ref. 1 when  $T = 300$  K and (b) for Case Ref. 2 when  $T = 900$  K.

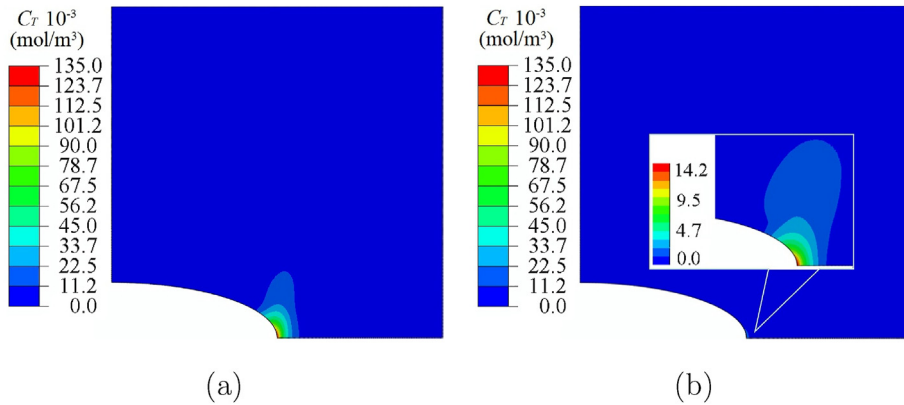


**Fig. 7** – Distribution of dislocation trapped hydrogen in the double notched specimen under tension (a) for Case Ref. 1 when  $T = 300$  K and (b) for Case Ref. 2 when  $T = 900$  K.

increase in temperature reduces the equilibrium constant  $K$  exponentially (c.f. Eq. (14)) from 1361.44 to 11.08. Therefore, the change in the equilibrium constant  $K$  overcompensates the effect of plastic strain increase, which results in a significant drop in the trapped hydrogen concentration when the temperature increases from 300 K to 900 K.

#### *Influence of average temperature for a non-uniform temperature field*

It remains to investigate the hydrogen transport under a non-uniform temperature distribution. We first investigate the distribution of  $C_L$  and  $C_T$  when the direction of concentration increase as prescribed by the concentration boundary conditions is aligned with that of temperature increase, i.e. Cases 1–3 with  $\eta < 0$ . Subsequently, Cases 4–6 with  $\eta > 0$  are studied when the direction of concentration increase is opposite to that of temperature increase.

For Cases 1, 2 and 3,  $\eta = -4$  K/mm while  $\bar{T}$  is equal to 400 K, 600 K and 800 K, respectively. For Case 1, the steady-state temperature and hydrostatic stress distributions are shown in Fig. 8a and Fig. 8b, respectively. Fig. 8 indicates how the temperature and stress vary in the cases under discussion. Fig. 9 illustrates the steady-state  $C_L$  distribution for Cases 1, 2

and 3 along with the result of Case Ref. 1 (uniform temperature) for comparison.

The comparison between Fig. 9a (Case Ref. 1) and Fig. 9b (Case 1) reveals that lattice hydrogen concentration  $C_L$  in Case 1 increases along the direction of temperature drop, towards the top surface of the domain and then suddenly drops due to the  $C_L = 0$  boundary condition prescribed at the top surface of the specimen. Moreover,  $C_L$  in Case 1 with  $T_{\text{Notch}} = 500$  K and  $T_{\text{Top}} = 300$  K has a peak value of 71.34 mol/m<sup>3</sup> compared to the peak value of 21.67 mol/m<sup>3</sup> in Case Ref. 1 with a uniform temperature of 300 K. This demonstrates that the temperature gradient is a major driving force for the transport of lattice hydrogen, which enables lattice hydrogen to diffuse from regions of high temperature to regions of low temperature. This phenomenon of temperature-induced lattice hydrogen transport is known as the Soret effect. Case 2 ( $\bar{T} = 600$  K) and Case 3 ( $\bar{T} = 800$  K) exhibit  $C_L$  distributions reminiscent to Case 1, except the temperature-induced lattice hydrogen transport is less pronounced as  $\bar{T}$  increases while  $\eta$  is kept fixed. This can be explained as follows; as the temperature increases, the coefficient  $Q^*/T$  in front of the term  $\nabla T$  in Eq. (8) decreases, leading to a less pronounced effect of the temperature gradient on the hydrogen transport.

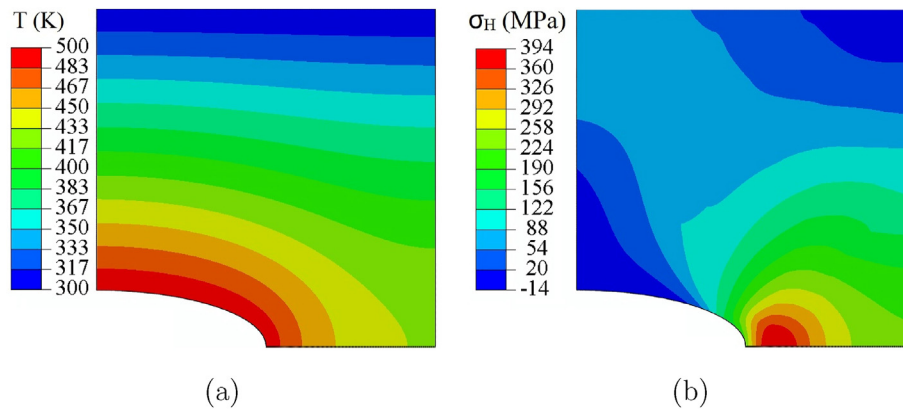


**Fig. 8 – (a) Steady-state temperature distribution and (b) hydrostatic stress distribution in the double notched specimen under tension for Case 1 with  $T_{\text{Notch}} = 500$  K and  $T_{\text{Top}} = 300$  K.**

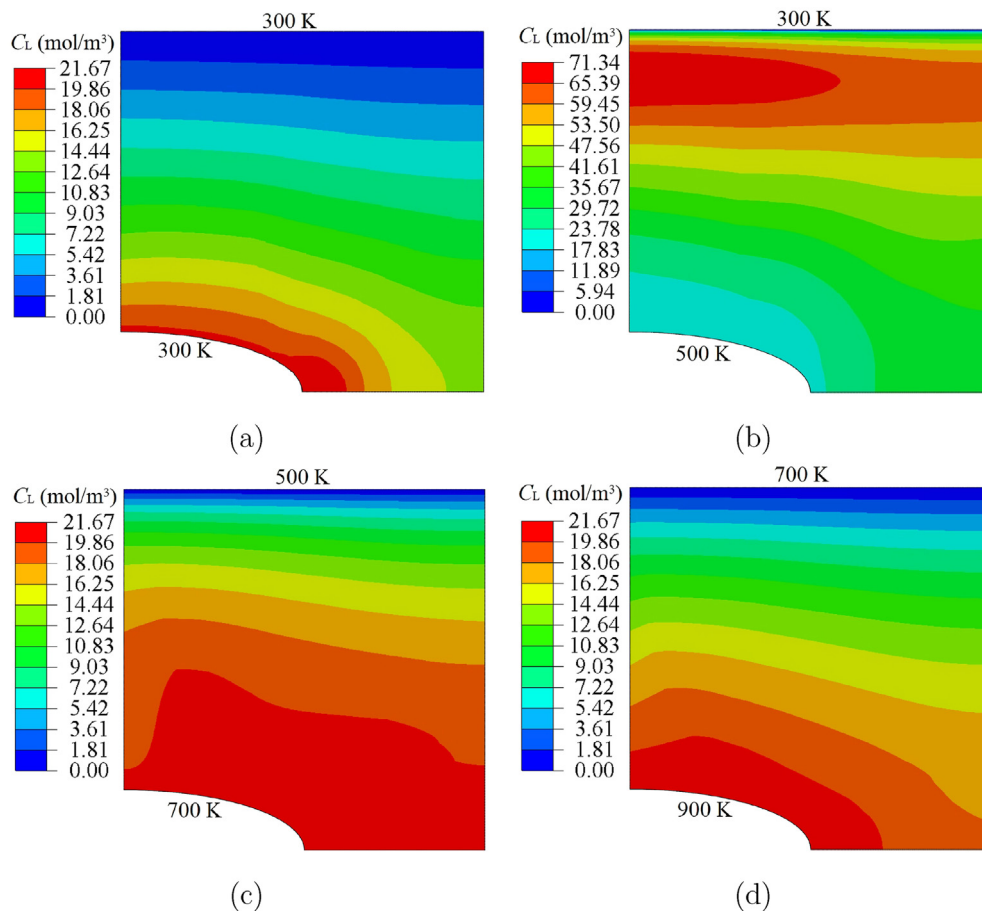


**Fig. 9 – Steady-state lattice hydrogen concentration in the double notched specimen under tension for (a) Case Ref. 1 with  $\bar{T} = 300$  K, (b) Case 1 with  $T_{\text{Notch}} = 500$  K and  $T_{\text{Top}} = 300$  K thus  $\bar{T} = 400$  K, (c) Case 2 with  $T_{\text{Notch}} = 700$  K and  $T_{\text{Top}} = 500$  K thus  $\bar{T} = 600$  K and (d) Case 3 with  $T_{\text{Notch}} = 900$  K and  $T_{\text{Top}} = 700$  K thus  $\bar{T} = 800$  K.**

The steady-state  $C_L$  profiles for Cases Ref. 1, 1, 2 and 3 along the X – axis and the Y – axis are plotted in Fig. 10a and Fig. 10b, respectively. For Case 1 with  $\bar{T} = 400$  K,  $C_L$  along the X – axis increases monotonically whilst for the other three cases, starting from around  $X = 35$  mm,  $C_L$  decreases gradually. This point along the X – axis where  $C_L$  peaks coincides with the location of the peak hydrostatic stress attained at the edge of

the plastic zone. Once again, it can be seen that as the average temperature  $\bar{T}$  increases, the degree of the temperature-induced lattice hydrogen transport diminishes. Meanwhile, an increase in average temperature  $\bar{T}$  also reduces the peak value of hydrostatic stress but increases the size of the plastic zone, i.e. pushes the peak  $\sigma_H$  position further along the X – axis, as depicted in Fig. 10c. The former is due to the

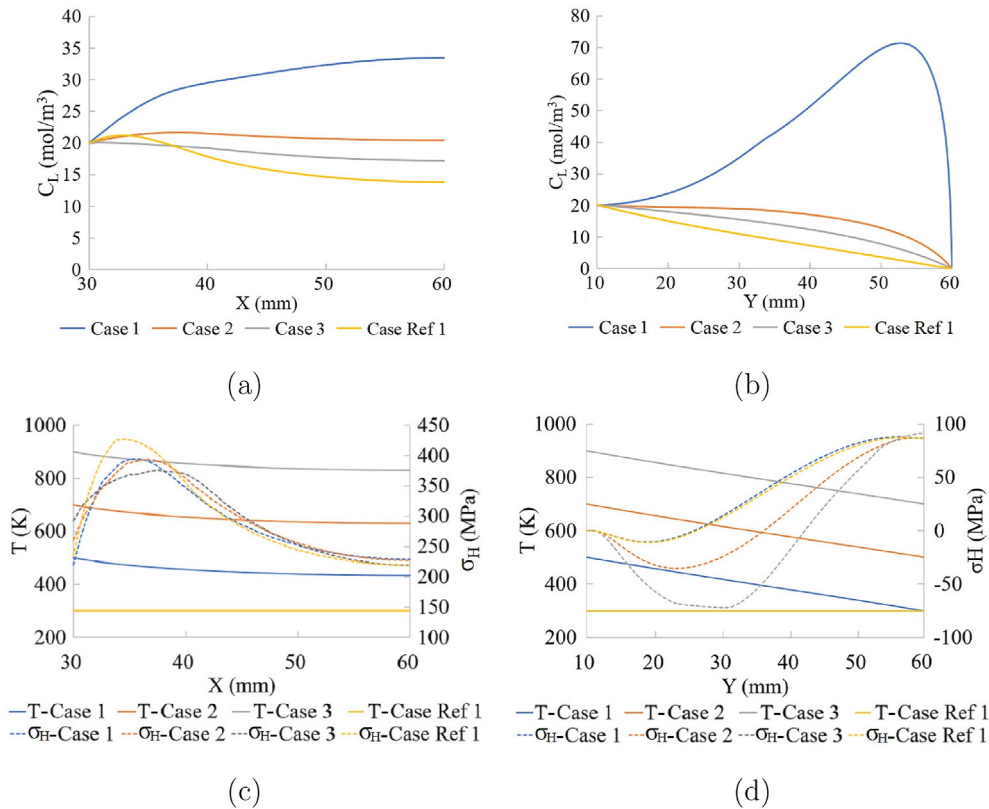


**Fig. 10** – Steady state lattice hydrogen concentration in the double notched specimen under tension (a) along the X – axis and (b) along the Y – axis, for Case 1, Case2, Case3 and Case Ref. 1. Temperature and hydrostatic stress in the double notched specimen under tension (c) along the X – axis and (d) along the Y – axis, for Case 1, Case2, Case3 and Case Ref. 1.

temperature dependence of Young's modulus  $E$  while the latter is due to temperature-dependent yield strength and plastic hardening accounted for in our calculations.

As discussed above, everything else being equal, the higher the temperature, the smaller the magnitude of the term  $\frac{Q_L^*}{T} \nabla T$  in Eq. (8). Therefore, increasing  $\bar{T}$  for a fixed value of  $\eta < 0$  leads to less temperature-mediated hydrogen diffusion and a more uniform  $C_L$  distribution along the X – axis. Moreover, since the effect of hydrostatic stress also reduces with increasing  $\bar{T}$ , the steady-state  $C_L$  distribution for Cases 2 and 3 are nearly uniform along the X direction.

In Fig. 10b, the steady-state  $C_L$  profile along the Y – axis is plotted. A steeper temperature gradient along the Y – axis (see Fig. 10d) emerges compared to that along the X – axis (Fig. 10c) for all cases with  $\eta < 0$ . A significant degree of temperature-induced lattice hydrogen transport is seen along the Y – axis for Case 1. The lattice hydrogen concentration along the Y – axis initially increases but then suddenly decreases due to the  $C_L = 0$  boundary condition prescribed at the top surface of the domain. The peak  $C_L$  value along the Y – axis in Case 1 ( $\bar{T} = 400$  K) indicates the degree of the temperature-induced lattice hydrogen

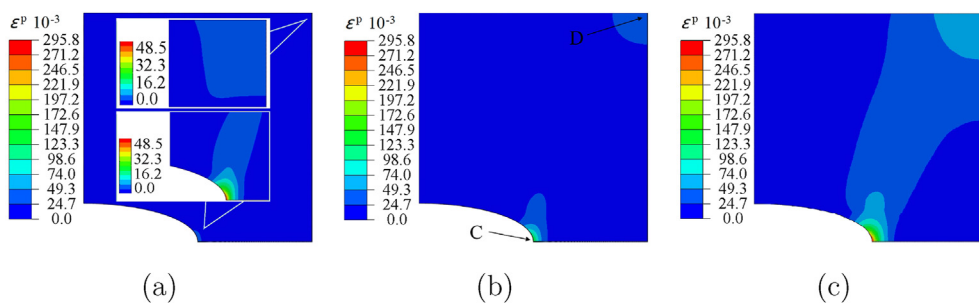


**Fig. 11** – Equivalent plastic strain distribution in the double notched specimen under tension for (a) Case 1 with  $T_{\text{Notch}} = 500$  K and  $T_{\text{Top}} = 300$  K thus  $T = 400$  K, (b) Case 2 with  $T_{\text{Notch}} = 700$  K and  $T_{\text{Top}} = 500$  K thus  $T = 600$  K and (c) Case 3 with  $T_{\text{Notch}} = 900$  K and  $T_{\text{Top}} = 700$  K thus  $T = 800$  K.

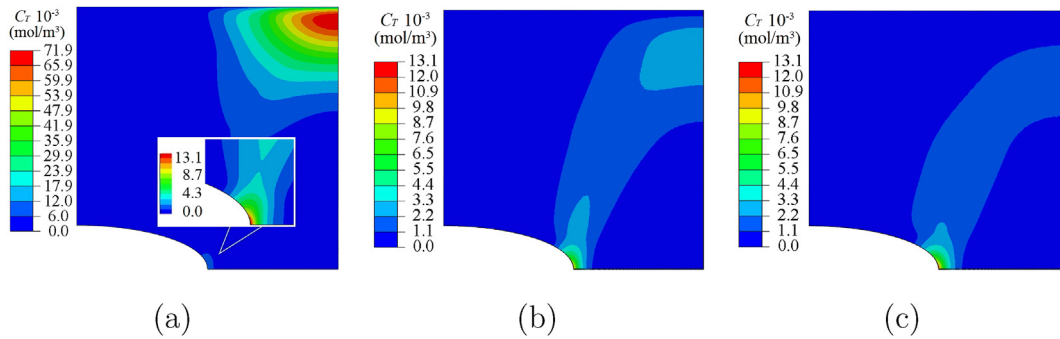
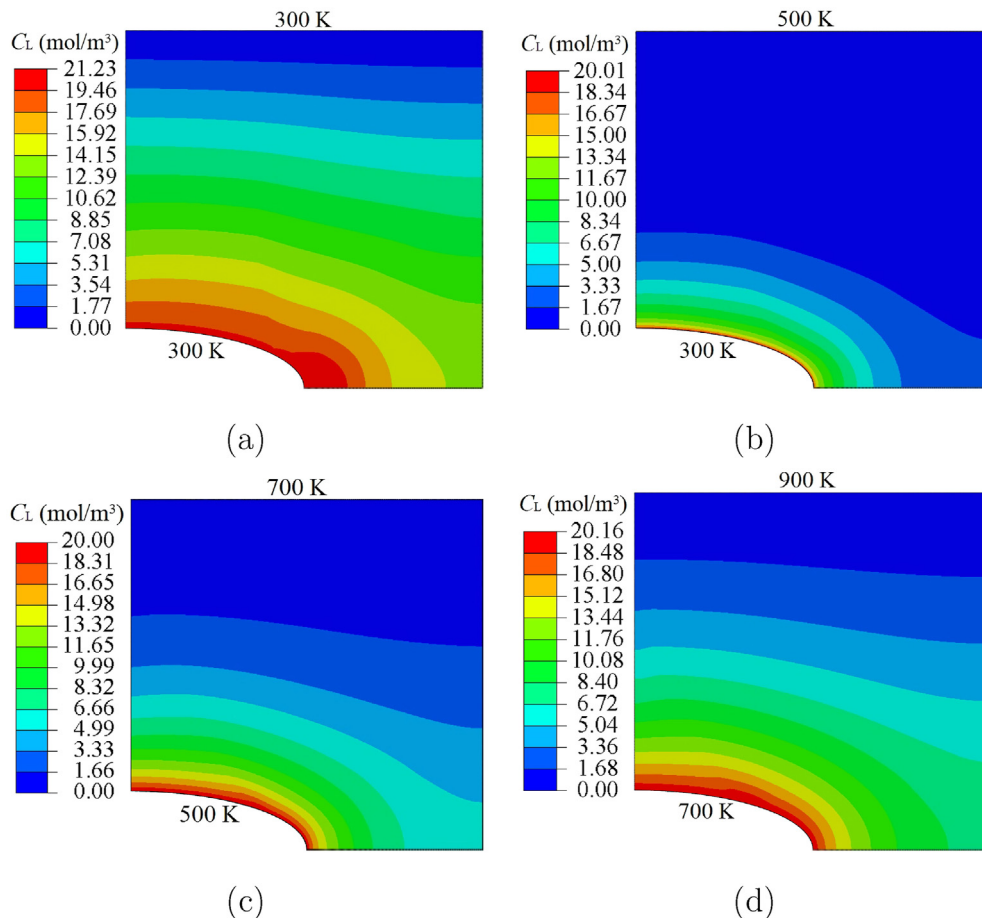


**Fig. 12** – Distribution of dislocation trapped hydrogen concentration in the double notched specimen under tension for (a) Case 1 with  $T_{\text{Notch}} = 500 \text{ K}$  and  $T_{\text{Top}} = 300 \text{ K}$  thus  $\bar{T} = 400 \text{ K}$ , (b) Case 2 with  $T_{\text{Notch}} = 700 \text{ K}$  and  $T_{\text{Top}} = 500 \text{ K}$  thus  $\bar{T} = 600 \text{ K}$  and (c) Case 3 with  $T_{\text{Notch}} = 900 \text{ K}$  and  $T_{\text{Top}} = 700 \text{ K}$  thus  $\bar{T} = 800 \text{ K}$ .

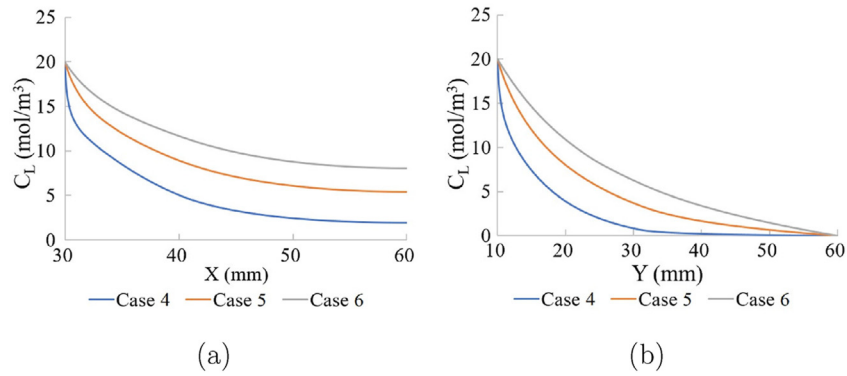
transport. In Case 2 ( $\bar{T} = 600 \text{ K}$ ) and Case 3 ( $\bar{T} = 800 \text{ K}$ ), the temperature-induced lattice hydrogen transport is more subtle as the influence of the temperature gradient diminishes by the rise in average temperature  $\bar{T}$ .

Fig. 11 illustrates the distribution of the equivalent plastic strain for Cases 1, 2 and 3. The plastic strain is observed near the notch root and the top right corner of the domain due to

high levels of Von Mises stresses in these regions. As the average temperature increases, the plastic strain at the notch root increases from  $\epsilon^p = 0.0485$  (for Case 1 with  $\bar{T} = 400 \text{ K}$ ) to  $\epsilon^p = 0.2958$  (for Case 3 with  $\bar{T} = 800 \text{ K}$ ) and the plastic zone expands. Moreover, the plastic deformation is also more prominent at the top right corner of the domain when  $\bar{T}$  rises. These observations can be attributed to the reduction in yield



**Fig. 13** – Distribution of lattice hydrogen in the double notched specimen under tension (a) for Case Ref. 1 with  $\bar{T} = 300 \text{ K}$ , (b) for Case 4 with  $T_{\text{Notch}} = 300 \text{ K}$  and  $T_{\text{Top}} = 500 \text{ K}$  thus  $\bar{T} = 400 \text{ K}$ , (c) for Case 5 with  $T_{\text{Notch}} = 500 \text{ K}$  and  $T_{\text{Top}} = 700 \text{ K}$  thus  $\bar{T} = 600 \text{ K}$ , and (d) for Case 6 with  $T_{\text{Notch}} = 700 \text{ K}$  and  $T_{\text{Top}} = 900 \text{ K}$  thus  $\bar{T} = 800 \text{ K}$ .

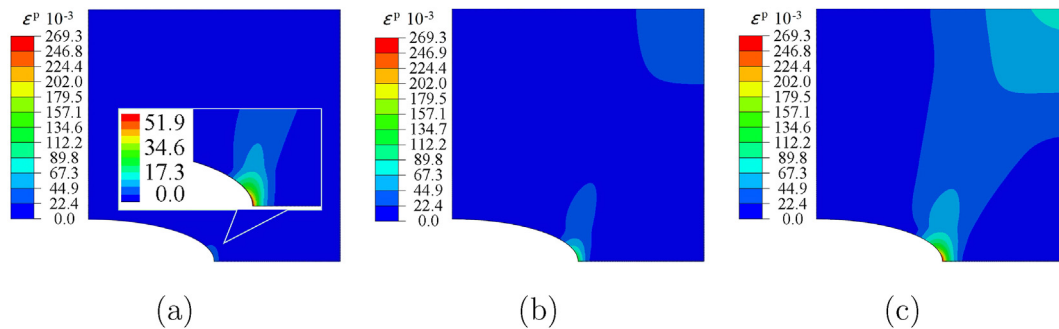


**Fig. 14** – Steady state lattice hydrogen concentration in the double notched specimen under tension (a) along the X – axis and (b) along the Y – axis, for Cases 4, 5 and 6.

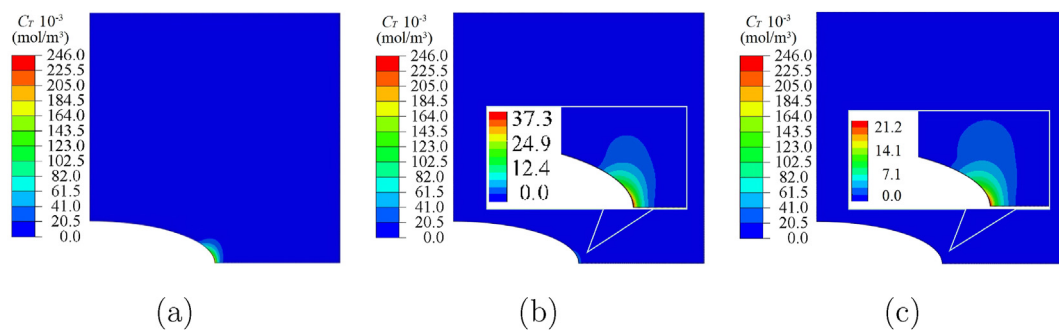
strength and the hardening slope of the material at higher temperatures.

Fig. 12 shows the trapped hydrogen concentration contour levels for Cases 1, 2 and 3. It is observed that  $C_T$  at the notch root increases from Case 1 to Case 2 and from Case 2 to Case 3 due to higher levels of plastic strain near the notch root with increasing  $\bar{T}$ . It is important to note that the local temperature in the vicinity of the notch root is the highest for Case 1 and lowest for Case 3. A higher value of temperature implies a higher equilibrium constant  $K$  that establishes the local equilibrium between  $\theta_L$  and  $\theta_T$  in Eq. (14), which in turn

decreases the local  $C_T$ . Upon comparing Fig. 12a for Case 1 and Fig. 12b for Case 2, the steady-state  $C_T$  value at the notch root for Case 2 appears lower, i.e. the effect of the equilibrium constant  $K$  prevails over the effect of plastic strain. However, upon comparing Fig. 12b for Case 2 and Fig. 12c for Case 3, the steady-state  $C_T$  at the notch root increases slightly for Case 3 which indicates the increase in the plastic strain is now more dominant than the increase in  $K$ . It can be seen in Eq. (15) that the degree of increase in  $K$  when increasing notch temperature from 500 K to 700 K is higher than that of increasing the notch temperature from 700 K to 900 K.



**Fig. 15** – Contour plots of plastic strain distribution in the double notched specimen under tension for (a) Case 4 with  $T_{\text{Notch}} = 300$  K and  $T_{\text{Top}} = 500$  K thus  $\bar{T} = 400$  K, (b) Case 5 with  $T_{\text{Notch}} = 500$  K and  $T_{\text{Top}} = 700$  K thus  $\bar{T} = 600$  K and (c) Case 6 with  $T_{\text{Notch}} = 700$  K and  $T_{\text{Top}} = 900$  K thus  $\bar{T} = 800$  K.



**Fig. 16** – Contour plots of dislocation trapped hydrogen concentration distribution in the double notched specimen under tension for (a) Case 4 with  $T_{\text{Notch}} = 300$  K and  $T_{\text{Top}} = 500$  K thus  $\bar{T} = 400$  K, (b) Case 5 with  $T_{\text{Notch}} = 500$  K and  $T_{\text{Top}} = 700$  K thus  $\bar{T} = 600$  K and (c) Case 6 with  $T_{\text{Notch}} = 700$  K and  $T_{\text{Top}} = 900$  K thus  $\bar{T} = 800$  K.

At the top right corner of the domain, a different trend is observed, i.e. steady-state  $C_T$  levels decrease with increasing  $\bar{T}$  from Case 1 to Case 2 and from Case 2 to Case 3 despite an increase in the local plastic strain. The reasons behind this phenomenon are twofold. Firstly, with the increasing  $\bar{T}$ , the equilibrium constant  $K$  is reduced exponentially. In addition to that, the strong temperature-induced lattice hydrogen

transport observed in Case 1 generates a drastic increase in the steady-state  $C_L$  (and hence  $\theta_L$ ) at the top right corner of the domain, which also contributes to the increase in local  $C_T$  c.f. Eq. (16). Previously we showed that this effect weakens with increasing  $\bar{T}$  since the temperature-induced lattice hydrogen transport becomes less prominent. This demonstrates that the temperature-induced hydrogen diffusion not only impacts

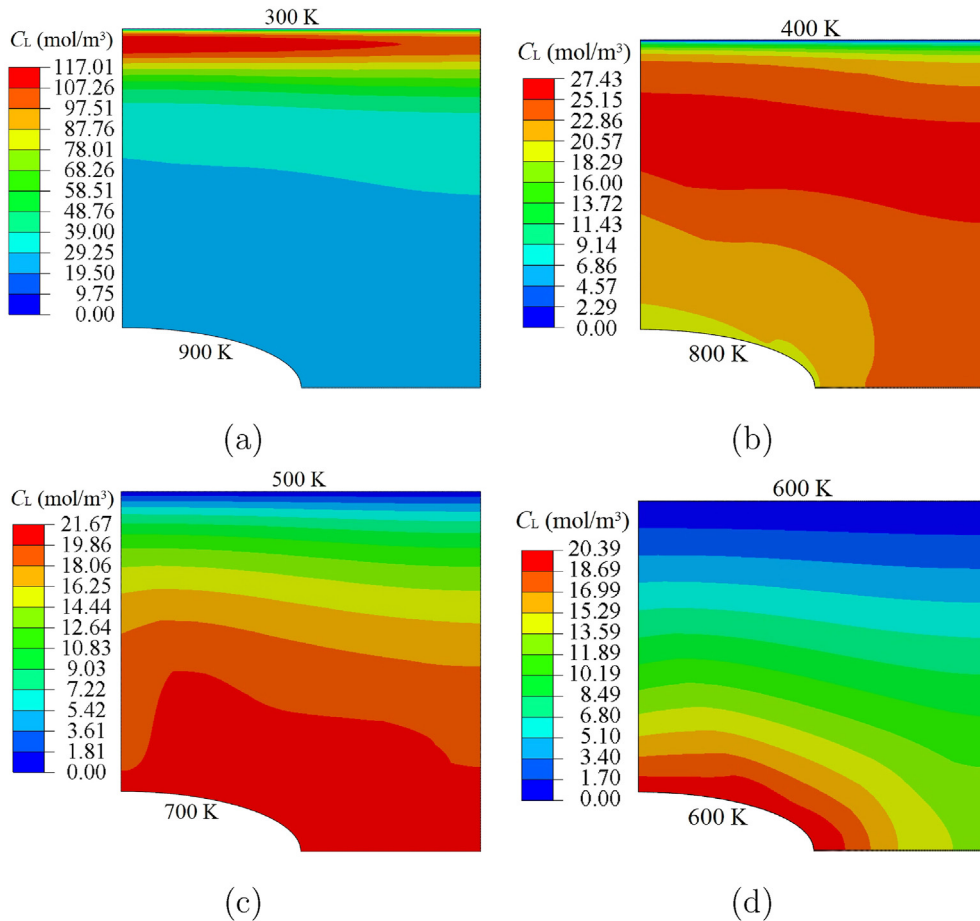


**Fig. 17** – Distribution of lattice hydrogen concentration in the double notched specimen under tension for (a) Case 7 with  $T_{\text{Notch}} = 900 \text{ K}$  and  $T_{\text{Top}} = 300 \text{ K}$  thus  $\eta = -12 \text{ K/mm}$ , (b) Case 8 with  $T_{\text{Notch}} = 800 \text{ K}$  and  $T_{\text{Top}} = 400 \text{ K}$  thus  $\eta = -8 \text{ K/mm}$ , (c) Case 9 with  $T_{\text{Notch}} = 700 \text{ K}$ ,  $T_{\text{Top}} = 500 \text{ K}$  thus  $\eta = -4 \text{ K/mm}$ , and (d) Case Ref. 3 with uniform temperature  $600 \text{ K}$  thus  $\eta = 0$ .

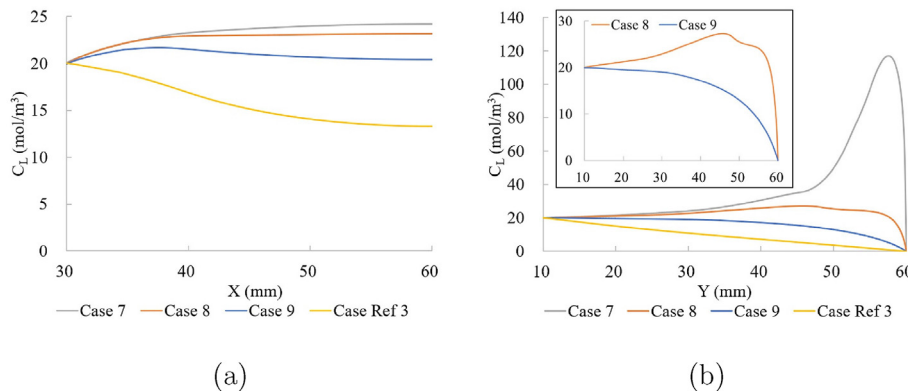


**Fig. 18** – Steady-state lattice hydrogen concentration in the double notched specimen under tension (a) along the X – axis and (b) along the Y – axis for Case 7, Case 8, Case 9, and Case Ref. 2.

the lattice hydrogen distribution but also indirectly affects the distribution of dislocation trapped hydrogen.

Next, we proceed with investigating the steady-state hydrogen distribution when the direction of the temperature increase is reversed. In Fig. 13, steady-state lattice hydrogen concentration distributions are given for Case Ref. 1, Case 4 ( $\bar{T} = 400$  K), Case 5 ( $\bar{T} = 600$  K) and Case 6 ( $\bar{T} = 800$  K). Temperatures prescribed as boundary conditions at the notch surface and the top surface of the specimen are also indicated in Fig. 13. Note that  $\eta = 4$  K/mm for Cases 4, 5 and 6 while  $\eta = 0$  for Case Ref. 1 with uniform temperature throughout the domain. For cases with  $\eta > 0$ ,  $C_L$  levels away from the notch surface vanish due to the temperature-induced lattice

hydrogen transport. This time the temperature gradient acts against the lattice hydrogen concentration gradient inhibiting diffusion. Since the degree of the temperature-induced lattice hydrogen transport reduces with increasing temperature, Case 4, with the lowest average temperature of  $\bar{T} = 400$  K, exhibits non-zero lattice hydrogen levels only in the immediate neighbourhood of the notch flank. In contrast, in Case 6, the temperature-induced lattice hydrogen transport is the weakest. Thus the steady-state  $C_L$  distribution is more similar to that of Case Ref. 1 with uniform temperature distribution. Moreover, the effect of the stress gradient is almost negligible. This is better demonstrated by visualising the steady-state  $C_L$  profiles along the  $X$  – and  $Y$  – axes in Fig. 14a and Fig. 14b,

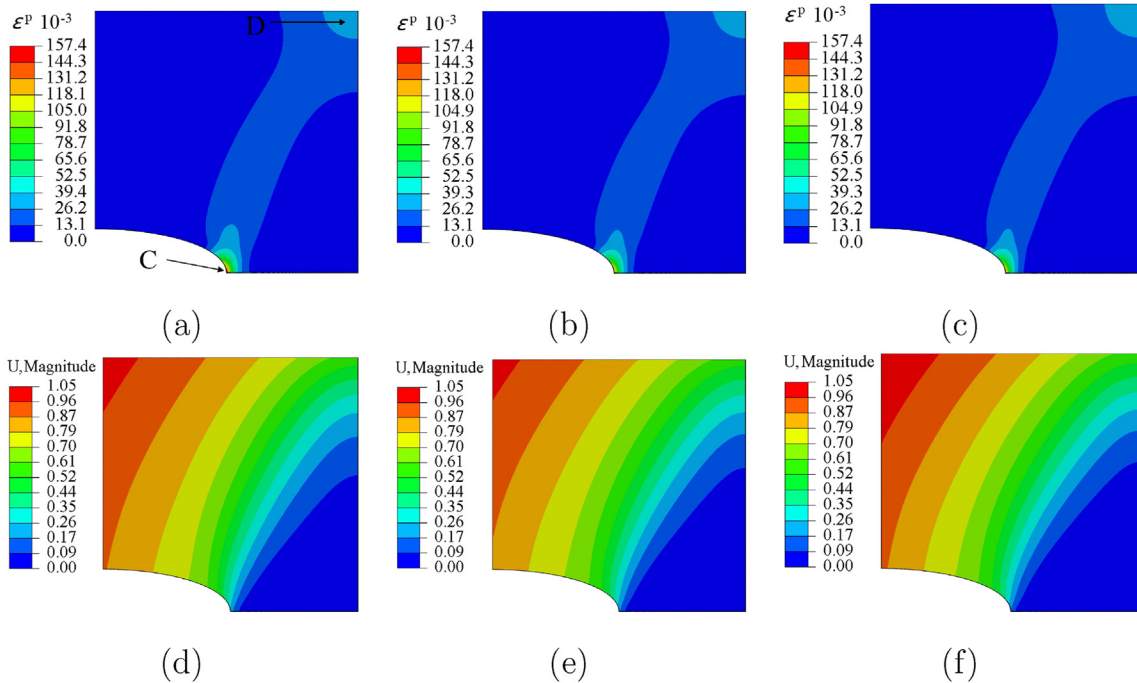


**Fig. 19** – Contour plots of equivalent plastic strain in the double notched specimen under tension for (a) Case 7 with  $T_{\text{Notch}} = 900$  K and  $T_{\text{Top}} = 300$  K thus  $\eta = -12$  K/mm, (b) Case 8 with  $T_{\text{Notch}} = 800$  K and  $T_{\text{Top}} = 400$  K thus  $\eta = -8$  K/mm, and (c) Case 9 with  $T_{\text{Notch}} = 700$  K and  $T_{\text{Top}} = 500$  K thus  $\eta = -4$  K/mm. Contour plots of magnitude of displacement in the double notched specimen under tension in mm for (d) Case 7 with  $T_{\text{Notch}} = 900$  K and  $T_{\text{Top}} = 300$  K thus  $\eta = -12$  K/mm, (e) Case 8 with  $T_{\text{Notch}} = 800$  K and  $T_{\text{Top}} = 400$  K thus  $\eta = -8$  K/mm, and (f) Case 9 with  $T_{\text{Notch}} = 700$  K and  $T_{\text{Top}} = 500$  K thus  $\eta = -4$  K/mm.

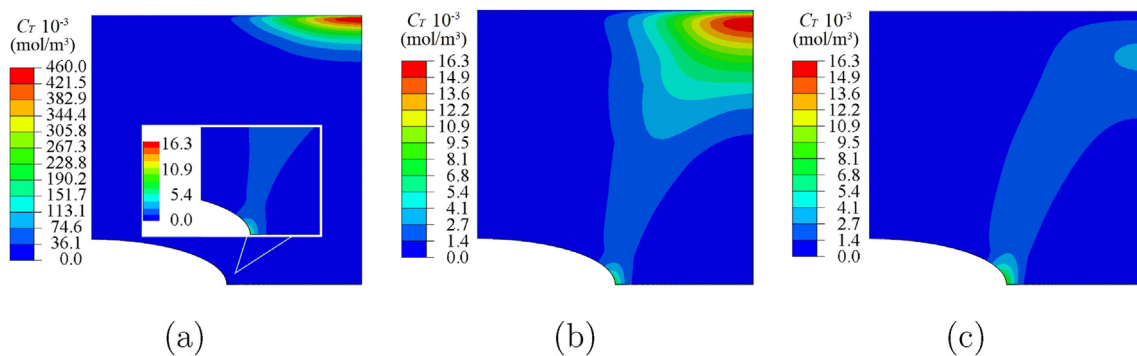


**Fig. 20** – Contour plots of dislocation trapped hydrogen concentration in the double notched specimen under tension for (a) Case 7 with  $T_{\text{Notch}} = 900$  K and  $T_{\text{Top}} = 300$  K thus  $\eta = -12$  K/mm, (b) Case 8 with  $T_{\text{Notch}} = 800$  K and  $T_{\text{Top}} = 400$  K thus  $\eta = -8$  K/mm, and (c) Case 9 with  $T_{\text{Notch}} = 700$  K and  $T_{\text{Top}} = 500$  K thus  $\eta = -4$  K/mm.

respectively. It can be observed that  $C_L$  decreases monotonically along both axes, for all cases plotted with  $\eta > 0$ , and the amount of decrease becomes more prominent when the temperature is lower due to a more pronounced temperature-induced lattice hydrogen transport as explained above.

Fig. 15 visualises the plastic strain distribution in Cases 4, 5 and 6. Similar to earlier results reported for Cases 1, 2 and 3, the localised plastic strain near the notch root and the top right corner increases due to thermal softening when  $\bar{T}$  increases. However, the amount of trapped hydrogen at the notch root reduces from  $0.246 \text{ mol/m}^3$  for Case 4 to  $0.021 \text{ mol/m}^3$  for Case 6, as shown in Fig. 16. Previously we showed that increasing  $\bar{T}$  reduces the equilibrium constant  $K$  and thus reduces  $C_T$  according to Eq. (16) even though the plastic strain increases with increasing  $\bar{T}$ . We also showed that the increase in  $K$  is more pronounced for lower temperatures. The  $C_T$  values at the top right corner of the domain simply vanish in the absence of any lattice hydrogen, i.e.  $\theta_L \approx 0$ .

### Influence of the degree of global temperature gradient

So far, we have focused on cases with a fixed global temperature gradient with  $|\eta| = 4 \text{ K/mm}$  for selected values of average temperature as indicated by  $\bar{T}$ . Next, we will study the degree

of the global temperature gradient. Cases 7, 8 and 9 are designed such that the average temperature is fixed to  $\bar{T} = 600 \text{ K}$  while  $\eta$  that characterises the global temperature gradient imposed on the domain for Case 7, 8 and 9 are  $-12 \text{ K/mm}$ ,  $-8 \text{ K/mm}$  and  $-4 \text{ K/mm}$  respectively. Note that the direction of temperature increase for  $\eta < 0$  is aligned with the direction of concentration increase prescribed by the concentration boundary conditions of the problem. Cases 10, 11 and 12 that will be discussed subsequently are also for  $\bar{T} = 600 \text{ K}$  while  $\eta > 0$ , i.e. the direction of temperature increase is reversed.

In Fig. 17,  $C_L$  distributions are depicted for a range of  $\eta$  values. For Case 7 with  $\eta = -12 \text{ K/mm}$ ,  $C_L$  first increases along the direction of the temperature drop, followed by a sudden drop near the top surface of the specimen since  $C_L = 0$  is prescribed at the top surface. A strong temperature-induced lattice hydrogen transport is observed as anticipated for the corresponding value of  $\eta$ . In Fig. 17b, a qualitatively similar  $C_L$  distribution is observed for Case 8 with  $\eta = -8 \text{ K/mm}$  albeit the temperature-induced lattice hydrogen transport is less prominent. In Fig. 17c  $C_L$  distribution for Case 9 is monotonically decreasing in the direction of the temperature drop since  $\eta = -4 \text{ K/mm}$  while  $\bar{T} = 600 \text{ K}$ . We note in passing that Case 9 is identical to Case 2 and discussed above. Previously

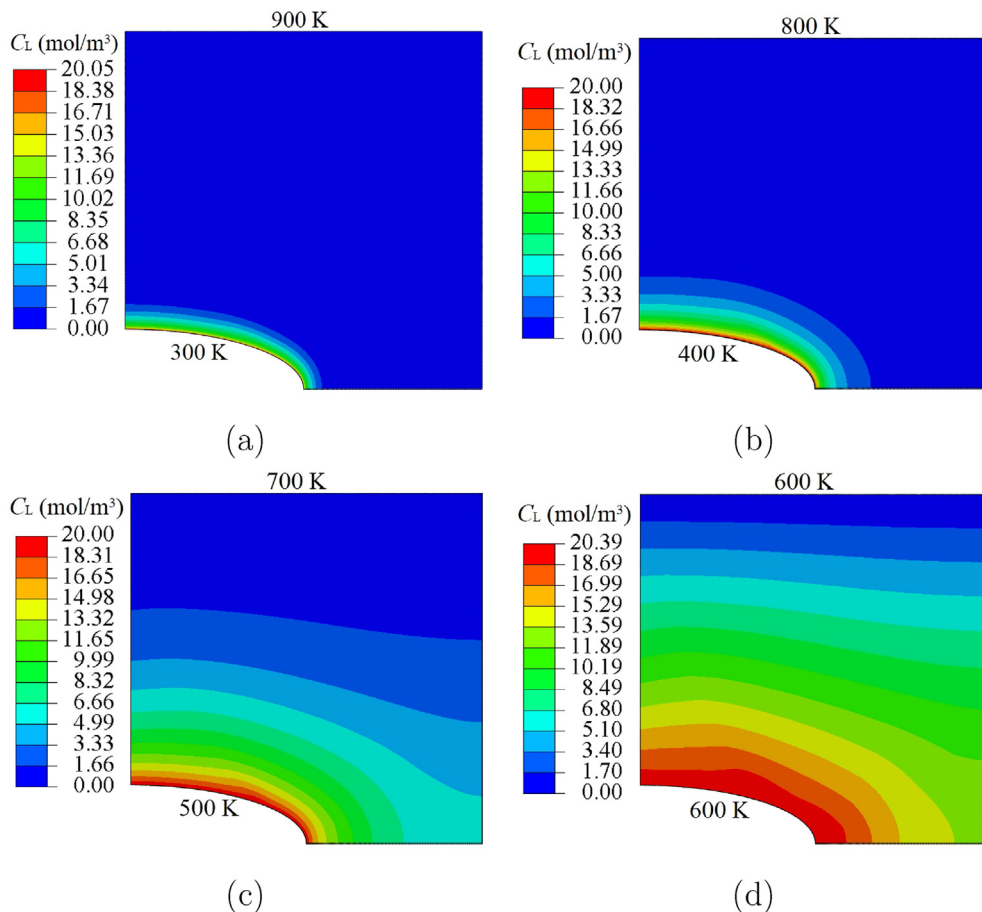


Fig. 21 – Distribution of lattice hydrogen in the double notched specimen under tension for Case 10 with  $T_{\text{Notch}} = 300 \text{ K}$  and  $T_{\text{Top}} = 900 \text{ K}$  thus  $\eta = 12 \text{ K/mm}$ , Case 11 with  $T_{\text{Notch}} = 400 \text{ K}$  and  $T_{\text{Top}} = 800 \text{ K}$  thus  $\eta = 8 \text{ K/mm}$ , Case 12 with  $T_{\text{Notch}} = 500 \text{ K}$  and  $T_{\text{Top}} = 700 \text{ K}$  thus  $\eta = 4 \text{ K/mm}$  and Case Ref 3 with uniform temperature  $600 \text{ K}$  thus  $\eta = 0$ .

we showed that the temperature-induced lattice hydrogen transport becomes less significant due to high  $\bar{T}$  for  $\eta = -4$  mm/K.

The effect of the temperature gradient is more clearly illustrated in Fig. 18 where the  $C_L$  distribution along the X – axis and Y – axis are given. The strong temperature-induced lattice hydrogen transport for Case 7 with  $\eta = -12$  mm/K becomes less prominent for Case 8 with  $\eta = -8$  mm/K and even more so for Case 9 when  $\eta = -4$  mm/K for  $\bar{T} = 600$  K.

Fig. 19 illustrates plastic strain distribution for Cases 7, 8 and 9. The plastic strain is mainly concentrated at the notch root and the top right corner of the domain due to the shape of the specimen and the applied loading. However, in contrast to

the results discussed above, plastic zone size and peak equivalent plastic strain values for Cases 7, 8 and 9 are similar. For instance,  $e^p$  at the notch root only decreases from 0.1574 for Case 7 to 0.1354 for Case 9. Recall that  $\bar{T} = 600$  K for Cases 7, 8 and 9. For Case 7, the temperature at the notch root is the highest ( $T_{\text{Notch}} = 900$  K), while the temperature at the top of the domain is the lowest ( $T_{\text{Top}} = 300$  K). The distribution of the magnitude of displacement for Cases 7, 8 and 9 are given in Fig. 19d–f, which illustrates the state of deformation for Cases 7, 8 and 9 are also very similar. Consequently, plastic strain distribution is virtually insensitive to the local temperature as long as  $\bar{T}$  is fixed.

In Fig. 20, the corresponding dislocation trapped hydrogen concentration distributions are given for Cases 7, 8 and 9. Near

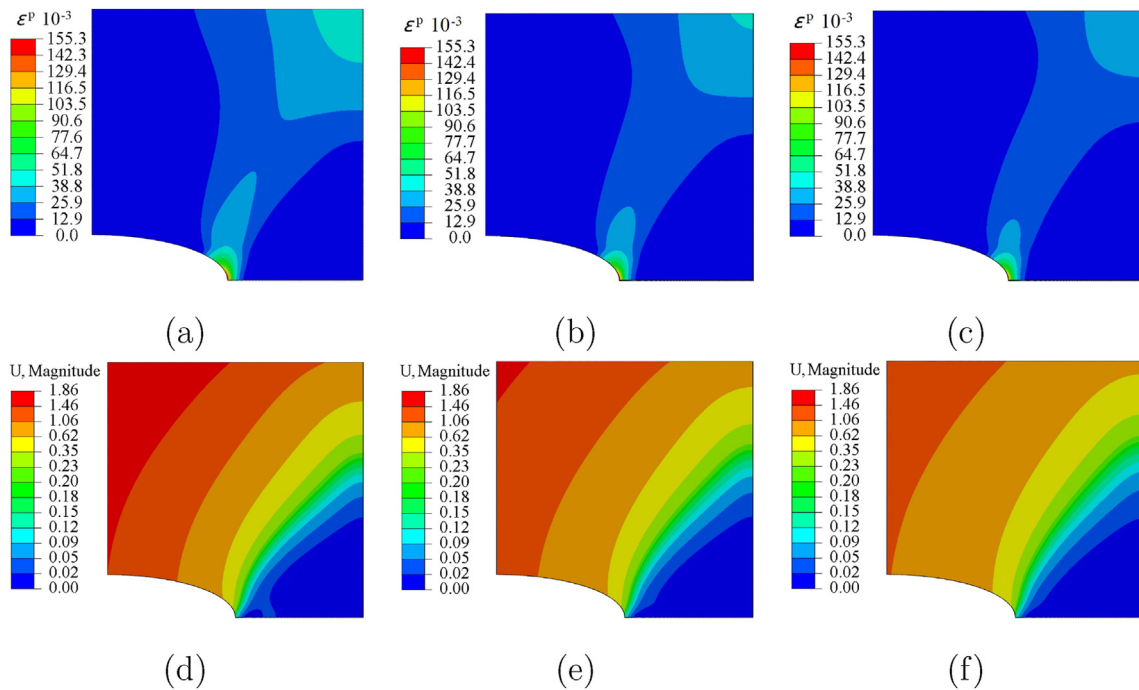


Fig. 22 – Contour levels of equivalent plastic strain in the double notched specimen under tension for (a) Case 10 with  $T_{\text{Notch}} = 300$  K and  $T_{\text{Top}} = 900$  K thus  $\eta = 12$  K/mm, (b) Case 11 with  $T_{\text{Notch}} = 400$  K and  $T_{\text{Top}} = 800$  K thus  $\eta = 8$  K/mm, and (c) Case 12 with  $T_{\text{Notch}} = 500$  K and  $T_{\text{Top}} = 700$  K thus  $\eta = 4$  K/mm. Contour levels of displacement magnitude in the double notched specimen under tension for (d) Case 10 with  $T_{\text{Notch}} = 300$  K and  $T_{\text{Top}} = 900$  K thus  $\eta = 12$  K/mm, (e) Case 11 with  $T_{\text{Notch}} = 400$  K and  $T_{\text{Top}} = 800$  K thus  $\eta = 8$  K/mm, and (f) Case 12 with  $T_{\text{Notch}} = 500$  K and  $T_{\text{Top}} = 700$  K thus  $\eta = 4$  K/mm.

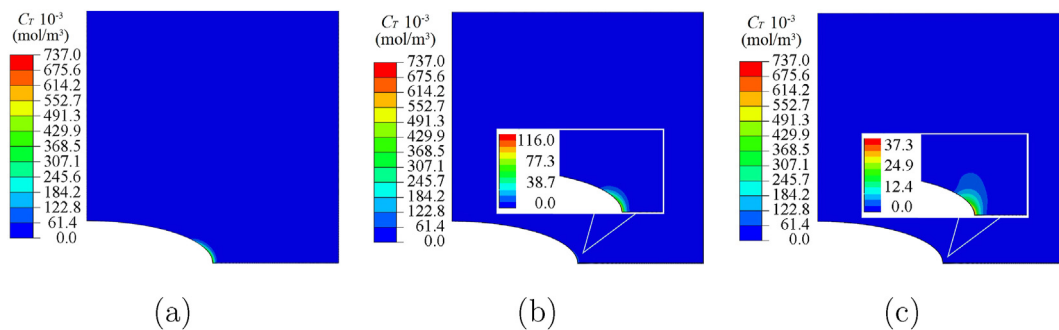


Fig. 23 – Contour levels of dislocation trapped hydrogen concentration in the double notched specimen under tension for (a) Case 10 with  $T_{\text{Notch}} = 300$  K and  $T_{\text{Top}} = 900$  K thus  $\eta = 12$  K/mm, (b) Case 11 with  $T_{\text{Notch}} = 400$  K and  $T_{\text{Top}} = 800$  K thus  $\eta = 8$  K/mm, and (c) Case 12 with  $T_{\text{Notch}} = 500$  K and  $T_{\text{Top}} = 700$  K thus  $\eta = 4$  K/mm.

the notch root,  $C_T$  levels are higher in Case 8 compared to Case 7, and  $C_T$  levels further increase for Case 9. Since plastic strain changes marginally, the remaining two factors are in play for the level of  $C_T$ . At the notch root, the equilibrium constant  $K$  between the occupancy ratios of lattice sites and dislocation sites for hydrogen creates the first-order effect. Consequently, hydrogen concentration trapped at dislocations increases from Case 7 to Case 8 and Case 8 to Case 9 at the notch root. At the top right corner of the domain, the manifestation of the  $C_T$  is predominantly dictated by the local  $C_L$  levels, given in Fig. 17. The highest level of  $C_T$  observed for Case 7 is primarily due to the very high  $C_L$  values attained at the top right corner because of the strong temperature-induced lattice hydrogen transport.

In Fig. 21, steady-state lattice hydrogen concentration distributions are given for Case 10 ( $\eta = 12$  mm/K), Case 11 ( $\eta = 8$  mm/K), Case 12 ( $\eta = 4$  mm/K) and Case Ref. 3 ( $\eta = 0$ ). The average temperature is the same for all these cases:  $\bar{T} = 600$  K. Temperatures prescribed as boundary conditions at the notch surface and the top surface of the specimen are also indicated in Fig. 21. Again, when the direction of the temperature increase is reversed, i.e.  $\eta > 0$ , the temperature-induced lattice hydrogen transport obstructs the diffusion of lattice hydrogen away from the notch surface in the double notched specimen. The steady-state  $C_L$  distributions reminiscent of Fig. 13 are obtained. It is seen that the degree of the temperature-induced lattice hydrogen transport directly correlates with the magnitude of  $\eta$  for a fixed value of  $\bar{T} = 600$  K.

Fig. 22 illustrates the plastic strain distribution for Cases 10, 11 and 12. The plastic strain distribution is localised in the vicinity of the notch root and the top right corner of the domain. The maximum amount of  $\epsilon^p$  decreases and the plastic zone shrinks from Case 10 with  $T_{\text{Notch}} = 300$  K to Case 11 with  $T_{\text{Notch}} = 400$  K and from Case 11 to Case 12 with  $T_{\text{Notch}} = 500$  K. This is counterintuitive at first glance since both yield strength and hardening decrease with increasing temperature. However, the plastic strain at the notch is a manifestation of the total state of deformation in the specimen. In Fig. 22d–f, the magnitude of the displacement field is plotted, and it is observed that Case 11 is enduring higher displacements than Case 12, and Case 12 is enduring higher displacements than Case 13. Note that  $T_{\text{Top}}$  is 900 K, 800 K and 700 K for Cases 11, 12 and 13, respectively. In Fig. 23, the corresponding trapped hydrogen concentration distributions are given. At the top right corner, no dislocation trapped hydrogen exists in the absence of lattice hydrogen (see Fig. 22) due to the temperature-induced lattice hydrogen transport. At the notch root, trapped hydrogen concentration is the highest for Case 11 as anticipated since both the plastic strain is the highest and the equilibrium constant  $K$  is the lowest.

### Implication for turbine blades

Our findings suggest that hydrogen embrittlement is likely to be of more concern at the locations where the temperature gradient and stress gradient are prominent in real applications such as gas turbine blades. If a fuel-rich mixture is used, the hydrogen gas surrounding the turbine blade is at a high

temperature, whilst the conformal cooling channels inside the turbine blades realise lower temperatures. Meanwhile, the centrifugal forces applied to the turbine blade will generate a non-uniform hydrostatic stress field due to the complex shape of the blade. The stress concentration around the cooling holes and the temperature difference between the outer surface of the blade and the internal surface of the cooling channel induce a risk of hydrogen embrittlement in the relatively low-temperature regions, although the stress concentration or plastic strain there is presumably not significant. This study also provides potential methods to avoid hydrogen embrittlement by weakening the temperature-induced transport of lattice hydrogen and redistribution of trapped hydrogen through increasing average temperature or changing the magnitude of the temperature gradient. They can, in principle, be realised by redesigning the internal cooling channels of the turbine blade.

### Conclusions

The combined effect of temperature and hydrostatic stress on steady-state lattice hydrogen diffusion and dislocation trapped hydrogen distribution is investigated using finite element analysis under various thermal boundary conditions using material properties of Alloy 690. The main conclusions are as follows:

1. Higher temperatures cause thermal softening and lead to a reduction of the hydrostatic stress levels, which results in less concentrated lattice hydrogen and lower trapped hydrogen concentrations.
2. The temperature-induced lattice hydrogen diffusion is more significant than the stress-induced one under the condition similar to the working environment of turbine blades. Up to two orders of magnitude increase in the lattice hydrogen concentration is predicted as in low-temperature regions compared with that in high-temperature regions, whilst the largest stress concentration only causes an increase in lattice hydrogen concentration by 6.15% at the elastic-plastic boundary.
3. The redistribution of dislocation trapped hydrogen results from the combined effects of stress and temperature, and it is influenced by both the magnitude and the direction of the global temperature gradient. When the direction of the temperature gradient is aligned with that of the initial hydrogen concentration gradient, the highest trapped hydrogen concentration occurs in a location where plastic strain is moderate, as long as the temperature-induced diffusion significantly increases the local lattice hydrogen concentration. Moreover, this redistribution of trapped hydrogen to regions with moderate plastic strain is promoted by the increased magnitude of the global temperature gradient. When the temperature gradient is reversed, trapped hydrogen will be limited to the location of the largest plastic strain.
4. Higher temperatures can significantly reduce dislocation trapped hydrogen concentration by weakening the influence of binding energy of hydrogen to dislocations, whilst higher plastic strain or lattice hydrogen concentration can only increase the trapped hydrogen concentration linearly.

## Declaration of competing interest

The authors declare that they have no known competing financial interests or personal relationships that could have appeared to influence the work reported in this paper.

## Acknowledgements

The authors greatly acknowledge the financial support provided within the Cohesion grant by the 3mE faculty of Delft University of Technology.

## Appendix A. Supplementary data

Supplementary data to this article can be found online at <https://doi.org/10.1016/j.ijhydene.2022.07.006>.

## REFERENCES

- [1] Cappelletti A, Martelli F. Investigation of a pure hydrogen fueled gas turbine burner. *Int J Hydrogen Energy* 2017;42:10513–23.
- [2] Öberg S, Odenberger M, Johnsson F. Exploring the competitiveness of hydrogen-fueled gas turbines in future energy systems. *Int J Hydrogen Energy* 2022;47:624–44.
- [3] Ratnakar RR, Gupta N, Zhang K, van Doorne C, Fesmire J, Dindoruk B, et al. Hydrogen supply chain and challenges in large-scale lh2 storage and transportation. *Int J Hydrogen Energy* 2021;46:24149–68.
- [4] Ishaq H, Dincer I, Crawford C. A review on hydrogen production and utilization: challenges and opportunities. *Int J Hydrogen Energy* 2021;47:26238–64.
- [5] Sofronis P, Liang Y, Aravas N. Hydrogen induced shear localization of the plastic flow in metals and alloys. *Eur J Mech Solid* 2001;20:857–72.
- [6] Bae K-O, Shin H-S, Baek U-B. Quantitative evaluation of hydrogen embrittlement susceptibility in various steels for energy use using an in-situ small punch test. *Int J Hydrogen Energy* 2021;46:20107–18.
- [7] del Busto S, Betegón C, Martínez-Pañeda E. A cohesive zone framework for environmentally assisted fatigue. *Eng Fract Mech* 2017;185:210–26.
- [8] Chen X, Zhou C, Zheng J, Zhang L. Effects of  $\alpha$  martensite and deformation twin on hydrogen-assisted fatigue crack growth in cold/warm-rolled type 304 stainless steel. *Int J Hydrogen Energy* 2018;43:3342–52.
- [9] Vaferi K, Nekahi S, Vajdi M, Moghanlou FS, Shokouhimehr M, Motallebzadeh A, Sha J, Asl MS. Heat transfer, thermal stress and failure analyses in a tib2 gas turbine stator blade. *Ceram Int* 2019;45:19331–9.
- [10] Sofronis P, McMeeking RM. Numerical analysis of hydrogen transport near a blunting crack tip. *J Mech Phys Solid* 1989;37:317–50.
- [11] Oriani RA. The diffusion and trapping of hydrogen in steel. *Acta Metall* 1970;18:147–57.
- [12] Balitskii A, Ivaskevich L. Assessment of hydrogen embrittlement in high-alloy chromium-nickel steels and alloys in hydrogen at high pressures and temperatures. *Strength Mater* 2018;50:880–7.
- [13] Moghanlou FS, Vajdi M, Motallebzadeh A, Sha J, Shokouhimehr M, Asl MS. Numerical analyses of heat transfer and thermal stress in a zrb2 gas turbine stator blade. *Ceram Int* 2019;45:17742–50.
- [14] Nekahi S, Vaferi K, Vajdi M, Moghanlou FS, Asl MS, Shokouhimehr M. A numerical approach to the heat transfer and thermal stress in a gas turbine stator blade made of hfb2. *Ceram Int* 2019;45:24060–9.
- [15] Johnson H, Morlet J, Troiano A. Hydrogen, crack initiation, and delayed failure in steel. *Trans. Met. Soc. AIME* 1958;212.
- [16] Troiano AR. The role of hydrogen and other interstitials in the mechanical behavior of metals, trans. *Am Soc Microbiol News* 1960;52:54–80.
- [17] Martínez-Pañeda E, del Busto S, Niordson C, Betegón C. Strain gradient plasticity modeling of hydrogen diffusion to the crack tip. *Int J Hydrogen Energy* 2016;41:10265–74.
- [18] Barrera O, Tarleton E, Tang H, Cocks A. Modelling the coupling between hydrogen diffusion and the mechanical behaviour of metals. *Comput Mater Sci* 2016;122:219–28.
- [19] Shang J, Zheng J, Hua Z, Li Y, Gu C, Cui T, Meng B. Effects of stress concentration on the mechanical properties of x70 in high-pressure hydrogen-containing gas mixtures. *Int J Hydrogen Energy* 2020;45:28204–15.
- [20] Metsue A, Oudriss A, Feaugas X. Hydrogen solubility and vacancy concentration in nickel single crystals at thermal equilibrium: new insights from statistical mechanics and ab initio calculations. *J Alloys Compd* 2016;656:555–67.
- [21] Maki H, Sato M. Thermal diffusion of hydrogen in zircaloy-2 containing hydrogen beyond terminal solid solubility. *J Nucl Sci Technol* 1975;12:637–49.
- [22] Oriani R. Thermomigration in solid metals. *J Phys Chem Solid* 1969;30:339–51.
- [23] Asaro RJ, Farkas D, Kulkarni Y. The soret effect in diffusion in crystals. *Acta Mater* 2008;56:1243–56.
- [24] Sawatzky A. Hydrogen in zircaloy-2: its distribution and heat of transport. *J Nucl Mater* 1960;2:321–8.
- [25] Varias A, Massih AR. Hydride-induced embrittlement and fracture in metals—effect of stress and temperature distribution. *J Mech Phys Solid* 2002;50:1469–510.
- [26] Quecedo M, Muñoz-Reja C, Avanzadas EI. A model for the thermally assisted diffusion of hydrogen in zirconium alloys and its fem solution. 2015.
- [27] Zielinski A. Hydrogen-assisted degradation of some non-ferrous metals and alloys. *J Mater Process Technol* 2001;109:206–14.
- [28] Barrera O, Cocks A. Computational modelling of hydrogen embrittlement in welded structures. *Phil Mag* 2013;93:2680–700.
- [29] Novak P, Yuan R, Somerday B, Sofronis P, Ritchie R. A statistical, physical-based, micro-mechanical model of hydrogen-induced intergranular fracture in steel. *J Mech Phys Solid* 2010;58:206–26.
- [30] Nagao A, Dadfarnia M, Somerday BP, Sofronis P, Ritchie RO. Hydrogen-enhanced-plasticity mediated decohesion for hydrogen-induced intergranular and “quasi-cleavage” fracture of lath martensitic steels. *J Mech Phys Solid* 2018;112:403–30.
- [31] Ayas C, Deshpande V, Fleck N. A fracture criterion for the notch strength of high strength steels in the presence of hydrogen. *J Mech Phys Solid* 2014;63:80–93.
- [32] Wang M, Akiyama E, Tsuzaki K. Effect of hydrogen on the fracture behavior of high strength steel during slow strain rate test. *Corrosion Sci* 2007;49:4081–97.
- [33] Ayas C, Fleck N, Deshpande V. Hydrogen embrittlement of a bimaterial. *Mech Mater* 2015;80:193–202.
- [34] Shishvan SS, Csányi G, Deshpande VS. Hydrogen induced fast-fracture. *J Mech Phys Solid* 2020;134:103740.
- [35] Lee W-S, Sun T-N. Plastic flow behaviour of inconel 690 super alloy under compressive impact loading. *Mater Trans* 2004;45:2339–45.

- [36] Kim H-S, Kim S-J. Influence of hydrogen and oxygen on the thermotransport of hydrogen in modified zircaloy-4. *Korean J Mater Res* 2003;13:473–7.
- [37] Mehrer H. *Diffusion in solids*. Berlin, Heidelberg: Springer; 2007.
- [38] Young Jr GA, Richey E, Morton DS. Hydrogen embrittlement in nuclear power systems. In: *Gaseous hydrogen embrittlement of materials in energy technologies*. Elsevier; 2012. p. 149–76.
- [39] Longhurst GR. The soret effect and its implications for fusion reactors. *J Nucl Mater* 1985;131:61–9.
- [40] Blaizot J, Chaise T, Nélias D, Perez M, Cazottes S, Chaudet P. Constitutive model for nickel alloy 690 (inconel 690) at various strain rates and temperatures. *Int J Plast* 2016;80:139–53.
- [41] GmbH VM. Vdm® alloy 690 material data sheet no. 2015. p. 4038.
- [42] Smuk S, Hänninen H, Jagodzinski Y, Tarasenko O, Aaltonen P. Comparison of hydrogen effects on alloy 600 and 690. In: *Ninth international symposium on environmental degradation of materials in nuclear power systems—water reactors*. Wiley Online Library; 1999. p. 59–68.
- [43] Lee B-S, Kim J-M, Kwon J-Y, Choi K-J, Kim M-C. A practical power law creep modeling of alloy 690 sg tube materials. *Nucl Eng Technol* 2021;53:2953–9.